Renewable Energy 259 (2026) 125011

Contents lists available at ScienceDirect

Renewable Energy

journal homepage: www.elsevier.com/locate/renene

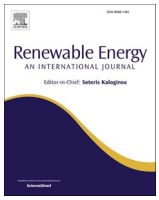

A novel machine learning-transfer function approach for estimating power absorption in floating wave energy converters

Mohammadreza Torabbeigi [a], Mohammad Adibzade [b], Arash Baharifar [b], Soroush Abolfathi [c,*]

[a] Faculty of Science and Engineering, Southern Cross University, Gold Coast, QLD, 4225, Australia
[b] Department of Civil and Environmental Engineering, Tarbiat Modares University, Tehran, Iran
[c] School of Engineering, University of Warwick, Coventry, UK

ARTICLE INFO

Keywords:
Renewable wave energy
Floating wave energy converter
Power estimation
Machine learning
Random forest
Gradient boosted regression tree
Multi-layer perceptron

ABSTRACT

Wave energy offers immense potential as a renewable energy source. However, accurately estimating the Total Absorbed Power (TAP) at various sites remains a significant challenge, requiring resource-intensive physical modelling and numerical simulations to capture the complex hydrodynamic behaviour of Wave Energy Converters (WECs) across different designs and wave conditions. To address this, we propose a novel, computationally efficient Machine Learning-Transfer Function (ML-TF) approach to estimate the TAP of Multi-Body Floating WECs (MBFWEC). The methodology integrates frequency-domain and time-domain analyses to generate a sparse dataset of MBFWEC responses under regular waves, which is used to train Machine Learning (ML) models. Wave height, wave period, and Power Take-Off (PTO) damping are the key inputs for predicting the Capture Width Ratio (CWR). Among the models tested, Multi-Layer Perceptron (MLP) model performed best (R^2 = 0.995). This model was then used to derive a high-resolution CWR dataset, with error margins within ±6.11 %, proving its reliability for out-of-range CWR predictions. To extend the model's applicability to irregular wave conditions, a Transfer Function (TF) was developed from the CWR dataset across a desired frequency range. The TAP was subsequently estimated based on the TF, site-specific wave power spectra, and the converter's effective length. Validation using time-history simulations in uni-modal and bi-modal sea states showed excellent accuracy (4 % maximum error), while achieving an 80 % reduction in computational cost. The methodology was further applied in a real-world case study using wave data from three locations in the northern Oman Sea, to evaluate the region's year-round power potential.

1. Introduction

Wave energy has gained significant attention as a renewable energy source due to its high-power potential compared to other renewable options such as wind, solar, and tidal energy. The global demand for sustainable energy solutions further highlights the importance of marine renewables. Projections suggest that by 2025, the share of wave energy in the global energy market will surge to $107 million, marking a substantial increase from its $47 million value in 2023 [1]. However, capturing and predicting wave energy remains a major challenge, especially for large-scale commercial wave farm applications [2]. Additionally, managing and storing wave energy is complex due to the irregular nature of wave climates in marine environments. Previous studies have emphasized the urgent need for a deeper understanding of wave energy dynamics and the enhancement of wave energy applications [3].

The design and optimization of Wave Energy Converters (WECs) are intrinsically linked to the specific characteristics of their deployment sites [4,5]. Since the efficiency of WEC energy capture mechanisms depends on sea state conditions, such as wave heights and periods, variations in these conditions can significantly influence WEC performance. Typically, statistical representations of sea states are depicted using scatter diagrams, with numerous cells representing the probability of each sea state's occurrence based on combinations of wave height and period. Evaluating WEC suitability across diverse marine sites requires assessing power performance against varying wave parameters. This assessment is then used to generate either a power matrix or a Capture Width Ratio (CWR) matrix, which describe the device's power

* Corresponding author.
E-mail address: Soroush.Abolfathi@Warwick.ac.uk (S. Abolfathi).

https://doi.org/10.1016/j.renene.2025.125011
Received 14 December 2024; Received in revised form 11 December 2025; Accepted 11 December 2025
Available online 13 December 2025

production or efficiency across different wave conditions. Comprehensive evaluations of WEC performance often require considerable time and resources, as the device must be adapted to accommodate the variability of wave conditions [6]. Furthermore, the power absorption efficiency of WECs is highly dependent on the performance of their Power Take-Off (PTO) damping systems, which determine how effectively the device converts wave motion into useable energy [7]. To fully harness the potential of WECs, it is essential to optimize PTO damping for each sea state condition. The large number of possible sea states necessitates generating a power matrix with high resolution, resulting in significant computational costs. Thus, developing an efficient methodology for generating the power matrix of WECs is crucial for advancing their design and optimization.

Numerical simulation techniques, such as computational fluid dynamics (CFD), frequency-domain, and time-domain modeling, can be employed to evaluate WEC performance under specific sea states and device configurations. In CFD simulations, the fundamental fluid dynamics equations, such as the Navier–Stokes equations, are solved numerically using either Lagrangian or Eulerian methods [8,9]. Although CFD modeling provides high-fidelity results, it is computationally expensive, limiting its use primarily to assessing WEC survivability rather than power output. Alternatively, frequency-domain and time-domain approaches, both rooted in potential flow theory, are widely utilized for assessing the power performance of WECs. Frequency-domain modeling efficiently evaluates frequency-dependent responses under linear conditions, while time-domain modeling captures nonlinear force components, providing more accurate power estimations. However, time-domain simulations require solving partial differential equations at each time step, leading to higher computational costs compared to frequency-domain approaches [10]. Although several methods have been proposed to address accuracy and computational cost issues [11,12], enhanced numerical approaches remain costly when conducting comprehensive assessments of WEC potential across various sea states and device configurations.

Over the past two decades, the development of various Machine Learning (ML) techniques and tools has led to the creation of efficient surrogate models that reduce computational costs. Recently, ML methods have gained significant traction in power prediction tasks. For instance, Zhou et al. [13] introduced Hybrid Physical-Machine Learning (HPML) models, which combine physical modeling with ML techniques to address power prediction challenges for wind turbines affected by wake effects in wind farms. Ren et al. [14] proposed an active learning Kriging approach for estimating spherical heaving point absorber (PA) power matrices, demonstrating that the method requires less than one-fifth of the simulations or experiments needed to construct the power matrix of WECs across all sea states, achieving a mean absolute percentage error of approximately 1 %.

Adibzade and Akbari [15] introduced a novel approach for evaluating floating WECs in complex sea states. Their study developed a Transfer Function (TF) across a range of wave frequencies to assess the power absorption capacities of FWECs. By multiplying the developed TF by the region-specific Mean Wave Power Spectrum (MWPS), the total extracted power for each proposed configuration could be determined. Since the TF is independent of sea states and relatively straightforward to apply, it provides an efficient means of evaluating or tuning FWEC devices for various regions, especially those with complex sea conditions.

However, a critical limitation of the TF approach lies in its dependence on a large number of high-fidelity numerical simulations to achieve sufficient frequency resolution across a wide range of PTO damping values. To address this challenge, we propose a hybrid framework that combines the physical interpretability of the TF method with the generalization capabilities of supervised ML models. Instead of replacing the TF with a purely data-driven model, our method enhances the TF resolution by training ML algorithms on a sparse dataset of numerical simulations. This integration allows for efficient estimation of power absorption over broad frequency and damping ranges with significantly reduced computational cost. This study utilizes response data from frequency-domain and time-domain modelling of a Multi-Body Floating WEC (MBFWEC). The data is then employed in supervised ML techniques, including Random Forest (RF), Gradient Boosted Regression Trees (GBRT), and Multi-Layer Perceptron (MLP), to obtain a CWR matrix. Frequency-domain modelling was conducted using ANSYS AQWA, while time-domain modelling utilized WEC-Sim, incorporating its batch run capability and the MATLAB Parallel Computing Toolbox (PCT). The dataset comprises the device's responses to a predefined set of regular waves with a limited range of heights and periods. Subsequently, the CWR matrix was calculated, and the most effective ML method was selected to develop the TF with the desired frequency resolution and PTO damping. The efficiency and accuracy of the proposed ML-TF model were validated by comparing its results with those obtained from direct simulations, ensuring reliable the Total Absorbed Power (TAP) estimations for the MBFWEC under real-life conditions. The total power absorption was then estimated using various sea states recorded in 2016 in the northern part of the Oman Sea.

2. Methodology

2.1. ML-TF modelling framework

The Wave Energy Spectrum (WES) serves as a fundamental benchmark for characterizing sea conditions, representing the distribution of wave energy across different frequencies within a specific geographical area. By integrating the region-specific WES with the device-specific TF, the TAP of a device under various sea states can be determined [15]. This process involves calculating the wave power spectrum from the WES over the same frequency range as the TF. However, obtaining a high-resolution TF typically requires extensive computational effort. Therefore, employing a data-driven approach can significantly alleviate this burden. In this study, we propose a novel Machine Learning–-Transfer Function (ML-TF) framework, which consists of four main stages, as illustrated in Fig. 1.

In the first stage (Step 1 in Fig. 1), a dataset is generated through numerical modeling to serve as input for the ML models in subsequent steps. For this purpose, the hydrodynamic performance of the proposed Multi-Body Floating Wave Energy Converter (MBFWEC) is evaluated using potential flow theory through both frequency-domain and time-domain modeling techniques. Frequency-domain analysis is conducted using the ANSYS AQWA module, which extracts key hydrodynamic coefficients such as excitation force, added mass, and radiation damping. These coefficients are then used to perform time-domain simulations that capture the MBFWEC's dynamic responses, including nonlinear forces, over a specified time period. The time-domain modeling is executed using WEC-Sim (Wave Energy Converter Simulator), an open-source software integrated with MATLAB's Parallel Computing Toolbox (PCT). This allows for evaluating the MBFWEC's power generation capabilities under a predefined set of regular waves with varying heights and periods (frequencies), creating a power window for each PTO damping setting. From these power windows, efficiency metrics such as the CWR are calculated and serve as inputs for the subsequent stages.

In the second stage (Step 2 in Fig. 1), supervised ML techniques, including Random Forest (RF), Gradient Boosted Regression Trees (GBRT), and Multi-Layer Perceptron (MLP), are employed to develop the most effective data-driven model. These ML models use wave height, frequency, and PTO damping as input features, with the CWR values as the target variable. Once the ML models are optimized, the best-performing model is selected to enhance the resolution of the CWR window for the desired frequency and PTO damping levels. Through this approach, a detailed assessment of MBFWEC efficiency across various wave conditions is achieved, reducing the computational cost associated with direct numerical simulations. The third stage involves the

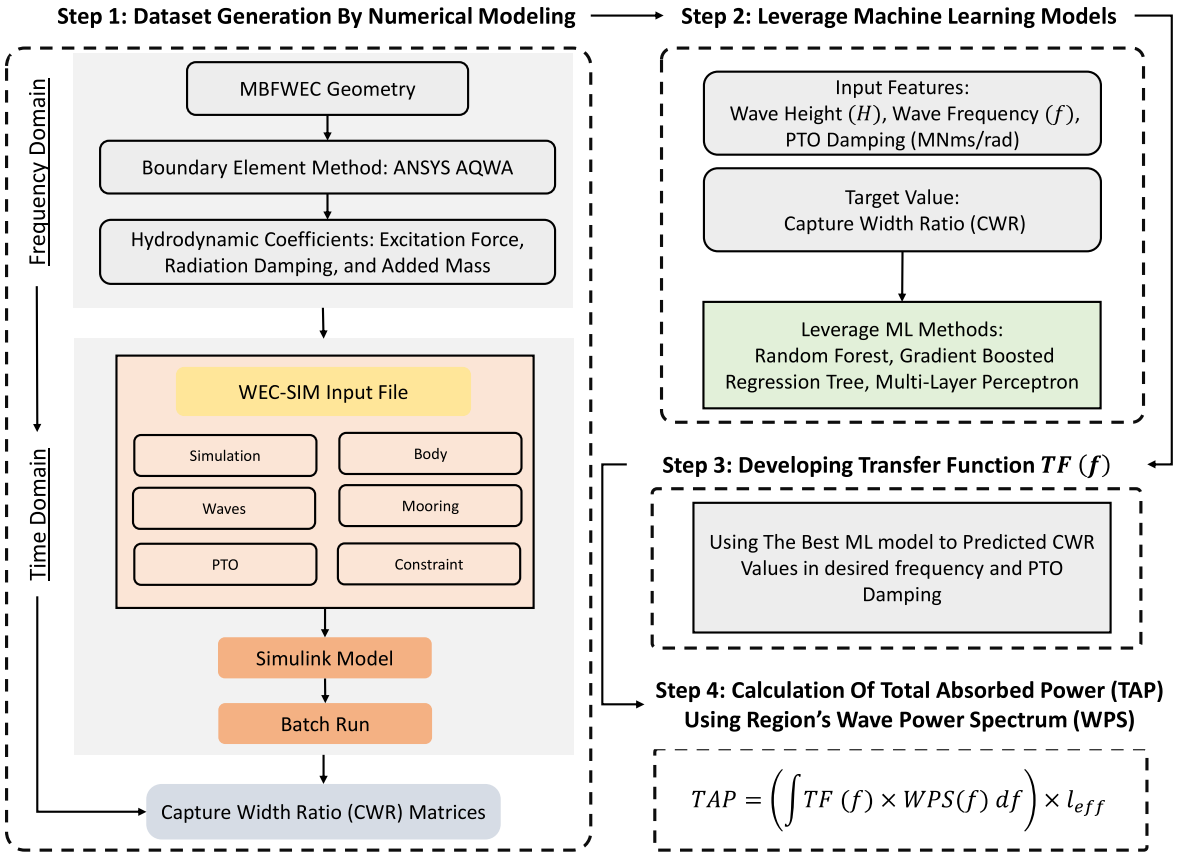

Fig. 1. Flowchart of the methodological approach developed in this study to determine the TAP using the ML-TF method.

development of TFs using the CWR windows obtained from the optimized ML model for the targeted frequencies and PTO damping settings. These TFs (discussed in Section 5.2) provide a more accurate and efficient means of evaluating the power absorption capabilities of the MBFWEC under diverse sea conditions. Finally, the fourth stage validates the efficiency and accuracy of the proposed ML-TF model by comparing its results with those obtained from direct numerical simulations. The TAP of the MBFWEC is calculated for region-specific single-peak and double-peak Wave Energy Spectra, demonstrating the model's robustness in capturing device performance under complex sea states.

2.2. Frequency-domain analysis

The performance of a FWEC is influenced by a multitude of factors, including its geometry, dimensions, and water depth, all of which directly affect its hydrodynamic coefficients. These coefficients encompass excitation force, added mass, and radiation damping. The excitation force coefficient determines the force generated by incident waves, crucially influencing the FWEC's potential power output. Added mass refers to the effective increase in weight of the floating member due to the surrounding moving fluid. It directly affects the device's response to wave forces and its natural frequency of oscillation. Radiation damping is the damping force resulting from waves generated by the FWEC itself as it oscillates through the fluid. Radiation damping influences the FWEC's motion, and the energy loss associated with the generated waves. Together, these hydrodynamic coefficients encapsulate the complex interactions among the device's components, significantly impacting their motion and overall efficiency. The total response of each component is determined by three primary factors: individual motion, mutual interaction between the central body (CB) and the floats, and the interference effects among floats in active degrees of freedom (DOFs).

The equation of motion of a floating body in frequency-domain, idealizing it for a single active DOF is expressed as follows:

$$-\omega^2 m\bar{z}(\omega) = \overline{F_{hd}}(\omega) + \overline{F_{hs}}(\omega) + \overline{F_{pto}}(\omega) + \overline{F_m}(\omega) \quad (1)$$

where $\bar{z}$ is a complex amplitude of the position, and m is the mass of the body. Hydrodynamic force $\overline{F_{hd}}$ is defined as:

$$\overline{F_{hd}}(\omega) = \overline{F_{ex}}(\omega) + \overline{F_{rd}}(\omega) \quad (2)$$

where $\overline{F_{ex}}$ and $\overline{F_{rd}}$ are excitation and radiation forces, respectively. $\overline{F_{ex}}$ is the sum of Froude-Krylov and diffraction forces. The radiation force is given by:

$$\overline{F_{rd}}(\omega) = -i\omega\, C(\omega)\bar{z}(\omega) + \omega^2 A_m(\omega)\bar{z}(\omega) \quad (3)$$

where $C(\omega)$ is the damping coefficient and $A_m(\omega)$ represents the added mass. The hydrostatic force $\overline{F_{hs}}$ denotes the restoring force in the form of buoyancy (or stiffness) of the system and is given as Eq. (4):

$$\overline{F_{hs}}(\omega) = -\rho g A_w \bar{z}(\omega) \quad (4)$$

where the hydrostatic force $\overline{F_{hs}}$ is a function of displacement $\bar{z}(\omega)$, g denotes gravity, ρ is the density of water, and A_w is water plane (or wet projected) area. The damping force induced by the PTO system which enables the device to extract energy, as a function of float's velocity $\dot{\bar{z}}(\omega)$ and damping coefficient C_{pto} in the active DOF, is given by:

$$\overline{F_{pto}}(\omega) = -i\omega\, C_{pto}\bar{z}(\omega) \quad (5)$$

The forces generated due to the presence of mooring cables are computed as an additional linear stiffness coefficient K defined as:

$$\overline{F_m}(\omega) = -K\,\bar{z}(\omega) \quad (6)$$

2.3. Time-domain analysis

To evaluate the time-domain responses of the MBFWEC system, we employed WEC-Sim—an open-source and extensively validated tool designed for the modeling of devices with hydrodynamic bodies, joints, constraints, Power Take-Off (PTO) systems, and mooring components. The WEC-Sim model used in this study was implemented in MATLAB/SIMULINK, leveraging the capabilities of the Simscape Multibody dynamics solver. Hydrodynamic data for the MBFWEC, which includes added mass, radiation damping, and wave excitation coefficients, were obtained from ANSYS AQWA using the Boundary Element Method (BEM). The BEM-derived hydrodynamic coefficients provide the device's response to incident waves for a predefined set of wave frequencies. Subsequently, this data is integrated into WEC-Sim to conduct time-domain simulations that account for the coupling of FWECs with PTOs and interactions with external bodies and forces [16]. Time-domain simulations are carried out by solving the governing equations of motion for the FWEC with six Degrees of Freedom (DOFs). These equations are formulated based on the methodology developed by Cummins et al. [17] for linear time-domain analysis and are expressed as:

$$(M+A_\infty)\ddot{Z}(t)+KZ(t)+\int_{-\infty}^{t} C_r(t-\tau)\dot{Z}(\tau)d\tau+C_{rot}\Delta\dot{\theta}(t)=\int_{-\infty}^{t}\eta(\tau)F_{ex}(t-\tau)d\tau+F_m \tag{7}$$

where M and A_∞ represent the total dry mass and added mass matrix at infinite frequency, respectively. K denotes the hydrostatic stiffness matrix at still water level, $\dot{Z}$ and $\ddot{Z}$ represent the time-dependent velocity and acceleration vectors of bodies, respectively. The state space time-invariant output matrix (C_r) provides the total memory effect of the radiation force, with τ denoting the time shift of convolution terms (radiation and excitation force). C_{rot} stands for rotational damping coefficient [Nms/rad] and $\Delta\dot{\theta}$ indicates the relative pitch velocity between CB and the float. F_{ex} denotes the wave excitation by impulse response function (IRF), η represents the free surface elevation, and F_m is the mooring force vector. This comprehensive formulation accounts for the intricate interactions between the MBFWEC and its surrounding marine environment, enabling a robust prediction of the system's dynamic response under a wide array of wave conditions. Such detailed modeling is essential for optimizing the performance of the MBFWEC and assessing its stability and energy capture efficiency under real-world sea states.

2.4. Supervised machine learning methods

This study implements three advanced supervised ML techniques, including Random Forest (RF), Gradient Boosted Regression Trees (GBRT), and Multi-layer Perceptron (MLP), to construct data-driven models for predicting CWR. The primary advantage of supervised learning is its ability to deliver highly accurate predictions on novel and unseen data, leveraging prior knowledge of labeled datasets [18–20]. The selection of these algorithms is based on their distinct capabilities in tackling various regression challenges and their proven success in prior research within the field. RF is widely recognized for its robustness and capacity to process large, high-dimensional datasets. By generating numerous decision trees in parallel and combining their results, RF effectively captures complex feature interactions and mitigates overfitting, making it highly reliable in diverse data environments [21]. In contrast, GBRT employs a sequential ensemble approach, where each tree is designed to correct the prediction errors of the preceding trees [22,23]. This iterative learning process allows GBRT to identify and adapt to subtle patterns in the data, thus enhancing predictive accuracy. As a result, GBRT excels in applications where the data structure is intricate, and the relationships between variables are less straightforward [24]. MLP, a neural network-based approach, is particularly suited for modeling non-linear relationships due to its complex architecture, which comprises multiple interconnected layers of neurons. This deep learning structure enables MLP to uncover intricate patterns and interactions within the data that might be overlooked by traditional tree-based models [25]. Moreover, MLP's flexibility in adjusting its structure (e.g., number of layers and neurons per layer) makes it adaptable for a wide range of hydrodynamic and ocean engineering problems. A comprehensive description of each ML model, including error analysis and feature importance, is presented in the following.

2.4.1. Random Forest (RF)

RF is an advanced ensemble ML algorithm designed to enhance predictive performance through the integration of multiple decision trees. RF leverages the principles of bagging (bootstrap aggregation) and the random subspace method to construct a robust predictive model [26]. During the training phase, the algorithm builds multiple decision trees, each using a randomly selected subset of the training data and features. The final prediction is obtained by averaging the outputs of these individual trees, thereby improving the model's overall accuracy and robustness [27]. The primary strength of RF lies in its ability to handle high-dimensional datasets and its intrinsic capability to reduce overfitting, which is a common limitation of single decision trees. By combining the predictions from multiple trees, RF reduces variance and increases stability, making it well-suited for diverse and complex data scenarios. This ensemble approach also enables RF to effectively manage noisy data and intricate interactions between features, rendering it a versatile tool for applications requiring high predictive accuracy.

In practice, the RF model development process involves several iterative steps to ensure optimal performance, as illustrated in Fig. 2 (a). First, bootstrap samples are generated from the original dataset, and individual decision trees are trained on these samples. During training, various metrics are used to evaluate model accuracy and effectiveness. If the model's performance is unsatisfactory, hyperparameters such as the number of trees, maximum tree depth, or feature selection criteria are adjusted, and the process is repeated. This iterative refinement continues until the model achieves the desired balance between bias and variance, resulting in a precise and reliable prediction model. Further details on RF methodology and its foundational concepts can be found in Ref. [27].

2.4.2. Gradient Boosted Regression Trees (GBRT)

Gradient Boosted Regression Trees (GBRT) is a powerful ML algorithm that builds upon the decision tree framework, initially introduced by Friedman [28]. The core principle behind GBRT is the concept of gradient boosting, where a series of simple models, referred to as "weak learners," are combined to create a strong predictive model. The algorithm starts by constructing a base model where all data points are assigned equal weights. After evaluating this initial model, GBRT iteratively adjusts by increasing the weights for instances that are misclassified while decreasing the weights for correctly classified instances. This adaptive weighting mechanism allows the model to focus more on the difficult-to-predict data points, enhancing its overall predictive accuracy.

The iterative process of gradient boosting in GBRT is executed in a stage-wise manner, refining the model at each step by sequentially adding regression trees to minimize residual errors. The update of the model at each stage m can be expressed as:

$$F_m(x)=F_{m-1}(x)+h_m(x) \tag{8}$$

where $h_m(x)$ represents the basic function at stage m, often a small regression tree of fixed size. Thus, the GBRT model is constructed by adding these weak learners sequentially to the existing ensemble. During each iteration m, a new tree $h_m(x)$ is fitted to the residuals from the

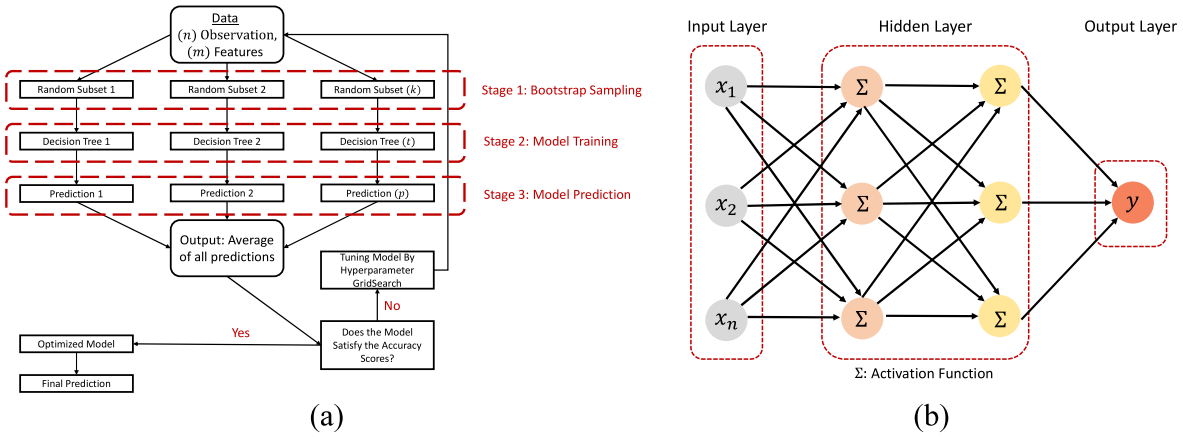

Fig. 2. The conceptual diagram for (a) Random Forest (RF), (b) Multi-Layer Perceptron (MLP) algorithm.

previous model, mathematically described as:

$$h_m(x) = y - F_{m-1}(x) \tag{9}$$

Here, y is the actual response, and $F_{m-1}(x)$ represents the predictions made by the previous iteration of the model. By focusing on these residuals, the algorithm systematically corrects the errors from earlier stages, thereby enhancing model accuracy over time. GBRT's ability to build models that learn complex patterns and relationships in the data makes it particularly effective for regression tasks in hydrodynamics and other engineering applications. Further theoretical insights and practical considerations regarding GBRT can be found in Friedman's seminal work [28].

2.4.3. Multi-Layer Perceptron (MLP)

The Multi-Layer Perceptron (MLP), a widely used variant of feed-forward neural networks, is structured with three primary layers: input, hidden, and output (Fig. 2 (b)). The fundamental building blocks of an MLP include interconnected neurons, biases, and weights that dictate the strength of the connections between neurons. In an MLP, each connection between nodes is associated with a weight, while each node, or neuron, has a designated bias. The learning process revolves around optimizing these weights and biases through training, typically utilizing algorithms like gradient descent. By iteratively refining these parameters, the MLP minimizes prediction errors and achieves optimal performance.

A distinctive feature of MLPs is the incorporation of activation functions at each node, which introduces non-linearity to the network. This non-linearity is crucial, as it enables the MLP to capture and model intricate patterns within the input data, which would otherwise be unattainable using purely linear models. The mathematical representation of an MLP Regressor (MLPR) is given by Ref. [29]:

$$f^{MLPR}(x) = c_r + \sum_q u_{qr} a_q(x) \tag{10}$$

where c_r represents the bias associated with the r^{th} output neuron, u_{qr} signifies the weight connecting the q^{th} neuron in the hidden layer to the r^{th} neuron in the output layer. The activation function of the hidden neuron, $a_q(x)$, is parameterized in terms of F as follows:

$$a_q(x) = F\left(d_q + \sum_p v_{pq} . x_p\right) \tag{11}$$

where d_q stands for the bias of the q^{th} hidden neuron, x_p is the input parameter, and v_{pq} denotes the weight linking the p th neuron in the input layer to the q^{th} neuron in the hidden layer. Through the use of these interconnected layers and non-linear activation functions, MLPs are capable of modeling complex relationships in data, making them highly effective for regression and classification tasks. Their adaptability and capacity for learning complex mappings have been extensively applied to diverse engineering problems, particularly where traditional methods struggle to capture the underlying relationships in data [29].

2.4.4. Grid search cross validation

In this study, Grid Search Cross-Validation (GSCV) is employed to optimize the hyperparameters of the ML models and ensure reliable and consistent predictions of the CWR values. The GSCV technique systematically evaluates a predefined set of hyperparameters by training and validating the model on multiple subsets of the dataset. By doing so, it identifies the optimal combination of hyperparameters that yield the highest model performance.

GSCV operates by dividing the entire dataset into K approximately equal-sized folds, with each fold serving as a validation set once, while the remaining folds are used for training the model. This process, known as K-fold cross-validation, is repeated K times, with a different fold utilized as the validation set during each iteration. This ensures that the model is rigorously tested on every subset of the data, providing a comprehensive evaluation of its generalization capability. The steps of cross-validation are as follows: First, the dataset is randomly divided into K folds of roughly equal-size. Then, the model is trained and evaluated K times. In each iteration, one fold is set aside as the validation set, while the remaining K-1 folds are used to train the model. Subsequently, performance metrics, specifically, Root Mean Squared Error (RMSE), are calculated for each fold. Finally, the overall RMSE is obtained by averaging the results across all K folds. The *GridSearchCV* class from the *Sklearn* library is used for hyperparameter tuning across all ML models.

2.4.5. Evaluation metrics

The efficacy of the proposed ML-based predictive models is rigorously assessed using a suite of comprehensive statistical error metrics, including the Coefficient of Determination (R^2), Root Mean Square Error (RMSE), Mean Absolute Error (MAE).

The Coefficient of Determination (Eq. (12)) is a statistical measure that quantifies the proportion of variance in the dependent variable that can be explained by the independent variables in a regression model. An R^2 value approaching 1 indicates that the model effectively captures the underlying variability in the dependent variable, while a value near 0 implies that the model explains little of the variation, indicating poor predictive performance. This measure is particularly critical in wave energy applications, where even modest prediction errors can have significant implications for system reliability, performance forecasting, and design optimization.

$$R^2 = 1 - \frac{\sum_{i=1}^{n}\left(y_i - y_{pred_i}\right)^2}{\sum_{i=1}^{n}(y_i - \bar{y})^2} \tag{12}$$

where y_i, y_{pred_i}, $\bar{y}$ are observed, predicted, and mean of all the observed values, respectively.

The Root Mean Square Error (RMSE) is determined as the square root of the average squared differences between predicted $\left(y_{pred_i}\right)$ and actual (y) values. As RMSE penalizes larger errors more heavily, it is particularly sensitive to significant deviations, making it an effective metric for assessing prediction accuracy in applications where large errors are especially detrimental, such as wave energy performance forecasting and system reliability assessments.

$$RMSE = \sqrt{\frac{1}{n}\sum_{i=1}^{n}\left(y_{pred_i} - y_i\right)^2} \tag{13}$$

Finally, the Mean Absolute Error (MAE) is computed as the average absolute difference between the predicted and actual values. Unlike RMSE, MAE treats all errors equally, regardless of their direction or magnitude, providing a clear and intuitive measure of the average prediction error in terms of its absolute value.

$$MAE = \frac{1}{n}\sum_{i=1}^{n}\left|y_{pred_i} - y_i\right| \tag{14}$$

Together, these metrics offer a comprehensive framework for evaluating different aspects of model performance, ensuring a robust and reliable assessment of the predictive capability of machine learning models in estimating the total absorbed power of floating wave energy converters.

3. Results and discussion

3.1. Numerical modeling and dataset

Single-body WECs, such as Point Absorbers (PAs), have a limited operational efficiency due to their narrow frequency bandwidth for wave energy capture. This narrow bandwidth necessitates continuous adjustments to maintain resonance with changing sea conditions [30]. In contrast, MBFWECs overcome this limitation by exploiting the relative motion between multiple interconnected bodies. This design enables a broader engagement with resonance frequencies, resulting in increased power absorption across a more diverse range of wave frequencies [31]. By distributing energy capture over a wider spectrum, MBFWECs are capable of harvesting energy more effectively from varied wave conditions. However, accurately modeling the complex interactions between multiple bodies in an MBFWEC system, each with multiple Degrees of Freedom (DOF), poses significant challenges [32]. Optimal energy conversion in these systems requires tailored damping ratios for each DOF of each body, along with variations in damping provided by the Power Take-Off (PTO) mechanism. Consequently, many multi-body WECs often operate with only one active DOF.

The configuration of the MBFWEC investigated in this study is depicted in Fig. 3. The system comprises a central, hollow cylindrical body (Central Body, or CB) that is connected to four curved tubular floats (F1-F4) via arms and hinge joints. This structural arrangement allows the relative motion between the CB and the floats, which is crucial for effective energy extraction. The hinge joints are aligned with the local y-axis of the floats, enabling rotational motion about the pitch angle. As the floats oscillate relative to the CB, the PTO system applies controlled damping, thereby converting the kinetic energy into useful power.

The CB is designed to be positively buoyant, ensuring it remains afloat, while stability is achieved by positioning the center of gravity below the center of buoyancy. To withstand extreme wave conditions such as those encountered during storms, the system is equipped with a "survival mode" in which vulnerable components can be fully submerged and locked in place, preventing structural damage and ensuring operational safety [33]. The geometric properties and design parameters

Table 1
Design parameters of the MBFWEC utilized in the numerical simulations of this study.

Design and operational parameters		MBFWEC
Water depth (m)		40
Density of seawater (kg/m^3)		1025
Height of the CB (m)		33
Radius of the CB (m)		3
Height of the floats		14
Width of the floats		4
Weight-CB (KN)		8370
Buoyancy-CB (KN)		8526
Weight and Buoyancy-Floats (KN)		5341
Center of Gravity-CB [X Y Z] (m)		[0, 0, −16]
Center of Gravity-Floats [X Y Z] (m)		[10.33, 0, −5.5]
Draft-CB (m)		30
Draft-Floats (m)		11
Freeboard-CB (m)		3
Freeboard-Floats (m)		3
Inertia-CB (kg.m^2)	I_{xx}	7.90×10^7
	I_{yy}	7.90×10^7
	I_{zz}	3.80×10^6
Inertia-Floats (kg.m^2)	I_{xx}	1.46×10^7
	I_{yy}	8.73×10^6
	I_{zz}	7.50×10^6
Length of the connecting arms (m)		6
Stiffness of mooring lines (KN/m)		3910
Pre-tension of each mooring line (KN)		39.1
Effective length of each float [parallel to wave] (m)		14.14
Effective length of each float [perp. to wave] (m)		5.76
Effective length of each configuration (m)		39.8

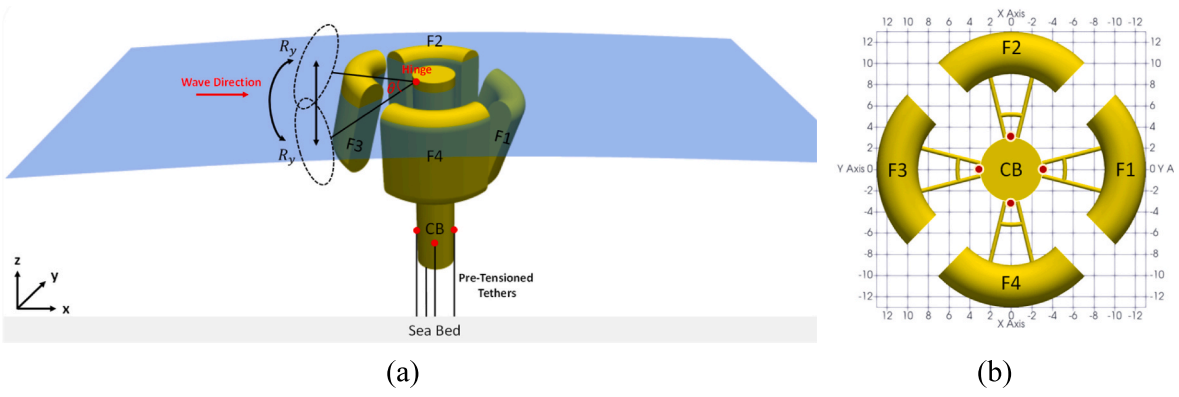

Fig. 3. Configuration of the MBFWEC: (a) schematic illustrating operational mechanisms; (b) plan view showing dimensions and scale.

of the MBFWEC configuration examined in this study are detailed in Table 1.

To determine the hydrodynamic coefficients of the MBFWEC, frequency-domain simulations were conducted using the AQWA-LINE module in ANSYS AQWA. This module solves the linearized potential flow problem under the classical assumptions of incompressible, inviscid, and irrotational fluid, combined with small-amplitude incident waves. The simulation involves both diffraction and radiation analyses. In the diffraction analysis, the structure is held fixed, while incident waves interact with the device, generating scattered wave fields. For the radiation problem, the device is allowed to oscillate in calm water within each of its six degrees of freedom (surge, sway, heave, roll, pitch, and yaw), producing corresponding radiated wave fields. The total hydrodynamic response is then obtained through the linear superposition of these components.

The boundary conditions applied in the simulations follow classical hydrodynamic theory and AQWA's standard formulation. A no-flux condition is enforced on the floating body's surface to prevent normal flow penetration, treating it as impermeable. On the free surface, a linearized combination of kinematic and dynamic boundary conditions is applied, consistent with the wave dispersion relation. The seabed is modeled as a flat, impermeable surface, while the far-field boundary employs the Sommerfeld radiation condition to ensure the proper dissipation of outgoing waves and eliminate artificial reflections [34].

The geometry of the MBFWEC was discretized using an unstructured quadrilateral panel mesh, as required by AQWA-LINE. Mesh refinement was concentrated in regions of high curvature, structural connections, and sharp edges where wave-body interactions are most sensitive. To ensure mesh independence, a convergence study was conducted using mesh densities ranging from 0.25 m to 0.5 m, with particular attention to the Response Amplitude Operator (RAO) in heave. Based on this analysis, a mesh size of 0.3 m was selected, as further refinement yielded negligible changes (less than 2 % variation in hydrodynamic coefficients). Panels were defined with accurately oriented normal vectors and centroid locations to facilitate precise evaluation of velocity potential surface integrals and associated hydrodynamic pressures.

Fig. 4 (a) shows the surface mesh applied to the MBFWEC geometry for the frequency-domain analyses, and Fig. 4 (b) presents the RAO variation in heave DOF for the CB under different mesh densities ranging from 0.25 m to 0.5 m.

Simulations were conducted over a frequency range of 0.01–0.8 Hz to comprehensively evaluate the MBFWEC's response under regular wave conditions. Incident wave directions varied from −180° to 180° in 30° increments, ensuring thorough coverage of all relevant approach angles. The primary outputs of the frequency-domain analysis include frequency- and direction-dependent wave excitation forces, radiation damping coefficients, and added mass, which serve as essential inputs for the subsequent dynamic response analysis of the MBFWEC.

In line with the assumptions inherent to linear wave theory and the AQWA framework, viscous effects and nonlinearities were neglected. The hydrodynamic centers and coordinate system were carefully aligned with the body-fixed reference frame, adhering to AQWA's standard conventions to ensure the consistency and accuracy of the results. For comparative analysis and to facilitate dimensionless representation, the hydrodynamic coefficients were normalized using the following expressions:

$$\widehat{F_{ex}} = \frac{\overline{F_{ex}}}{\rho g} \tag{15}$$

$$\widehat{A_m} = \frac{A_m}{\rho} \tag{16}$$

$$\widehat{C_{rd}} = \frac{C_{rd}}{\rho \omega} \tag{17}$$

where $\widehat{F_{ex}}$, $\widehat{A_m}$, and $\widehat{C_{rd}}$ represent the normalized hydrodynamic excitation force, added mass, and radiation damping coefficients, respectively. In these equations, ρ denotes the water density, g is the acceleration due to gravity, and ω is the wave frequency. These normalized coefficients correspond to the selected Degrees of Freedom (DOFs) for the analysis. Although hydrodynamic coefficients are computed for all DOFs of the MBFWEC system, only the heave and pitch DOFs are considered active in the configuration analysed in this study. Fig. 5 illustrates the normalized hydrodynamic coefficients computed for the heave DOF, providing insights into the frequency-dependent response characteristics of the system.

In WEC-Sim, each component of the MBFWEC is modeled using Simulink blocks within the MATLAB environment. The various interacting parts, such as floating members and the Central Body (CB), are represented as distinct hydrodynamic bodies. Connections are established between these components to facilitate multi-body interactions, allowing the system to simulate complex dynamics within the MATLAB/Simulink framework. The dynamic response of the MBFWEC is further integrated with mooring blocks, constraint blocks, and rotational Power Take-Off (PTO) blocks, which define linear PTO damping coefficients and act as rotational hinges in the system.

The influence of regular waves on the hydrodynamic behaviour and optimal settings of the PTO system can be effectively captured using this modelling framework. However, predicting the performance of a

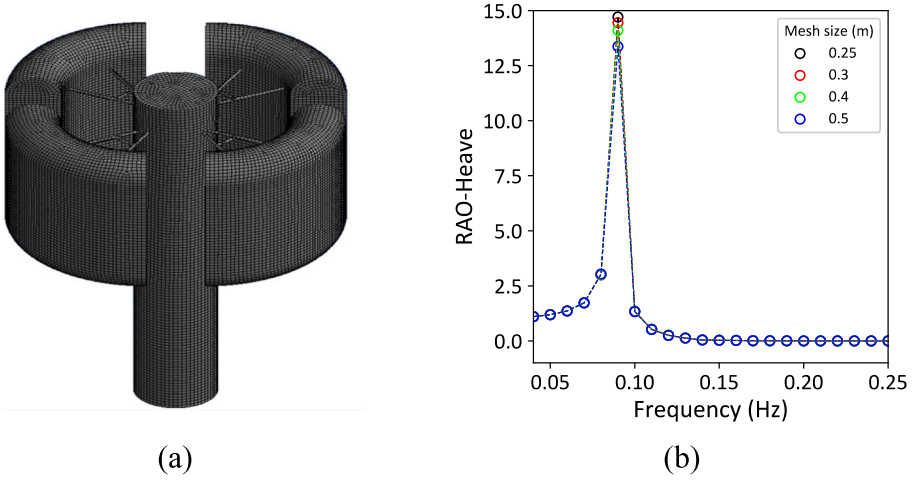

Fig. 4. **(a)** Surface mesh generated on the MBFWEC geometry used in the frequency-domain analyses. **(b)** Variation of the RAO in heave for the CB under different mesh densities ranging from 0.25 m to 0.5 m.

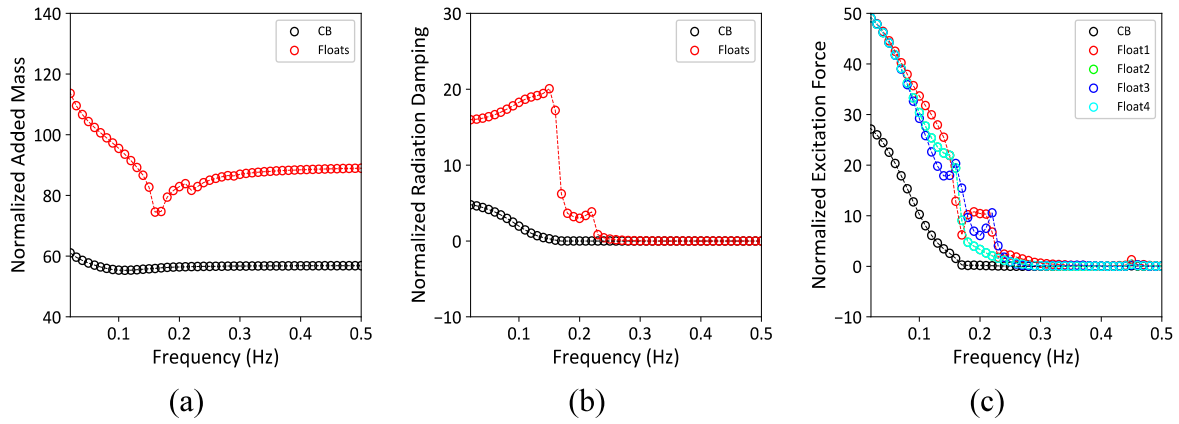

Fig. 5. Computed hydrodynamic forces for MBFWEC (a) Normalized added mass, (b) Normalized radiation damping, and (c) Normalized excitation force.

Floating Wave Energy Converter (FWEC) under realistic sea conditions, characterized by irregular and complex wave states, presents a significant challenge. In this study, time-domain simulations were performed to establish baseline data for ML models and ultimately develop a TF capable of estimating the TAP generated by the device in response to real sea waves. To achieve this, a predefined set of regular wave conditions was constructed, encompassing a comprehensive range of wave heights and periods. This dataset included 352 wave components, comprising 16 distinct wave heights (spanning from 0.1 m to 1.6 m) and 22 different periods (ranging from 2 s to 20 s, along with additional periods of 30 s, 40 s, and 50 s). Each wave component was simulated independently for the MBFWEC using WEC-Sim's batch run capability, which enabled consecutive simulation of all 352 components. Furthermore, MATLAB's parallel computing feature was employed to expedite the simulations, leveraging multiple processor cores to execute simulations simultaneously.

Each simulation was run for a duration of 500 s, using a time step of 0.005 s to ensure high-resolution results. The incident wave angle of approach was maintained at a constant 180° for all scenarios. Consequently, Float 3 (F3) was positioned as the first member, and Float 1 (F1) as the last member facing the wavefront, while Floats 2 and 4 were symmetrically placed as side floats, yielding identical modeling results due to their symmetry relative to the approaching wave angle. The entire MBFWEC configuration (Fig. 3) was subjected to six separate batch runs, each corresponding to a different level of PTO damping, ranging from 6 to 24 MNms/rad.

The PTO system employed in the MBFWEC device operates on a rotational basis, harnessing energy through the relative pitch motion between the CB and the floats. Consequently, the time-averaged power output per float, under regular wave conditions, can be expressed as:

$$P_i = \frac{1}{T}\int_0^T C_{rot}\left(\dot{\theta}_{CB} - \dot{\theta}_f\right)^2 dT \tag{18}$$

where C_{rot} (hereinafter C) is the rotational damping coefficient [Nms/rad], and $\left(\dot{\theta}_{CB} - \dot{\theta}_f\right)$ is the relative velocity of pitch angle between the CB and the floating body. Hence, with four floats, the total mean power absorbed by the proposed MBFWEC can be determined as:

$$\overline{P} = \sum_{i=1}^{4} P_i \tag{19}$$

The absorption length (L_b), also known as the Capture Width (CW) of the device, represents the ratio of the mean power absorbed P (in W) by the device to the power of the incident wave P_{wave} (in W/m), and is defined as follows [35]:

$$CW = \frac{P}{P_{wave}} \tag{20}$$

CW denotes the width of a wave crest fully absorbed by a WEC. However, the CWR is more suitable for assessing a WEC's hydrodynamic efficacy. The CWR provides a measure of the percentage of wave power that is effectively captured and converted by the device as waves propagate through the system. It is mathematically expressed as:

$$CWR = \frac{CW}{L_{eff}} * 100 \tag{21}$$

where L_{eff} represents the characteristic dimension encompassing the width of all components actively engaged in the energy absorption process from waves. For instance, when a platform incorporates multiple WECs, performance is adjusted based on the number of installed WECs. In such cases, the active width is defined as the width of each individual WEC. Therefore, l_{eff} can be determined as the sum of the effective length of all floating members:

$$l_{eff} = \sum_{j=1}^{m} L_{eff_j} \tag{22}$$

where m denotes the number of floating members.

Fig. 6 illustrates the CWRs obtained for a sample batch run, corresponding to a Power Take-Off (PTO) damping of 10 MN/m. The figure provides a grid of values that represent the hydrodynamic efficiency of the MBFWEC device for each wave height and period combination within the predefined window. In the figure, red indicates regions of higher efficiency, whereas blue signifies areas of lower efficiency. Additionally, the CWR distributions were generated for five other PTO damping values to create a comprehensive dataset for ML model development. CWR windows for the other damping values are described in the Supplementary Information (Fig. S1).

Following the outlined numerical modeling methodology, a total of 2112 simulations were performed (see Table 2). This includes six batch runs, each consisting of 352 simulations, covering 16 different wave heights and 22 periods for regular wave conditions. Each batch run, executed using MATLAB's Parallel Computing Toolbox (PCT) on an Intel® Core™ i7-11700K processor, required 2420 s, resulting in a cumulative simulation time of approximately 14,520 s (about 4 h). Fig. 7 presents the frequency distribution curve of the CWR values obtained from all 2112 simulations, providing insight into the overall hydrodynamic performance of the MBFWEC system.

3.2. Leveraging machine learning models

This section presents a comparative analysis of three ML models,

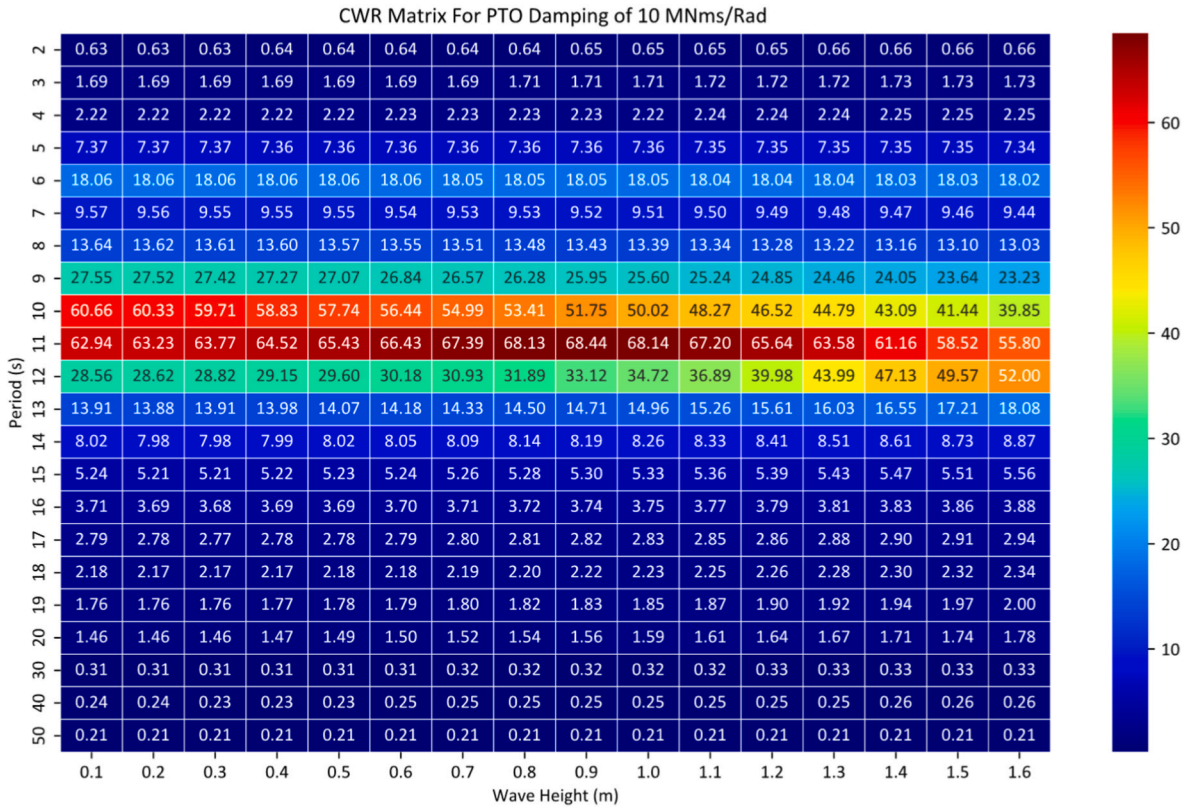

Fig. 6. Numerically generated CWR matrix for MBFWEC with PTO Damping of 10MNms/rad.

Table 2
Input ranges for wave height, wave period, and PTO damping used to generate the database for ML.

Properties	Input Range	No. of Scenarios	Total No. of Simulation
Wave Height (m)	0.1–1.6 (0.1 m Interval)	16	2112
Wave Period (s)	2-20 (1 s Interval) 30, 40, 50 s	22	
Damping (MNms/Rad)	6-10-14-18-22-24	6	

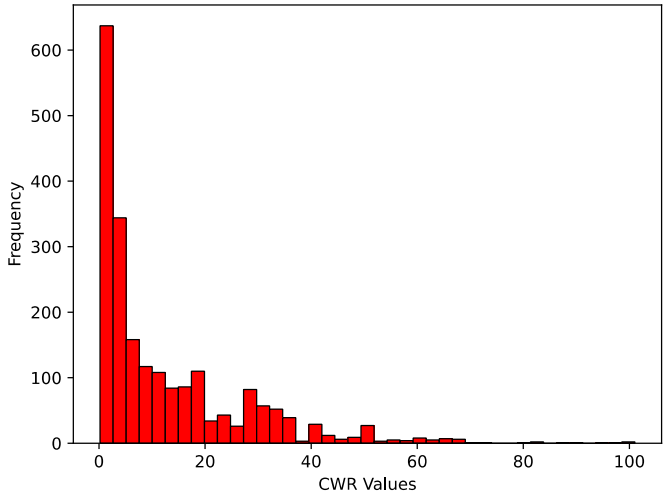

Fig. 7. Distribution of CWR values in the numerical modeling dataset, utilized for ML models.

including RF, GBRT, and MLP, for predicting the CWR of the MBFWEC. All models were developed and implemented using the Scikit-Learn library, adhering to the operational framework illustrated in Fig. 8. The data obtained from the numerical simulations (see Table 2) was split into input and output features. The input features consisted of wave height (H), wave frequency (f), and PTO damping coefficients, while the output feature was the CWR value of the MBFWEC.

During the preprocessing stage, scaling techniques were employed to standardize the input features for all ML models. This step is crucial, as unnormalized data can cause the algorithms to converge more slowly or, in some cases, fail to converge entirely. To normalize the input data, the *MinMaxScaler* class from *Scikit-Learn* was used. Once standardized, the dataset was partitioned into training and testing sets, with 70 % of the data used for training and the remaining 30 % reserved for testing, ensuring an unbiased evaluation of model performance.

In the subsequent stage, hyperparameters were tuned to optimize the performance of each ML model. Each algorithm type has a unique set of hyperparameters that significantly influence its behaviour during training. For the MLP model, hyperparameters like '*hidden_layer_sizes*' define the number of neurons in each hidden layer, directly affecting the model's capacity to capture complex patterns. The activation function, such as '*ReLU*', governs how the input signal is transformed as it passes through the network. The optimization algorithm, specified by the solver parameter, minimizes the loss function, with '*adam*' being a popular choice due to its adaptive learning rate. Additional parameters like '*batch_size*', '*learning_rate*', and '*max_iter*' control the frequency of model updates, the step size during optimization, and the maximum number of iterations, respectively.

Fig. 9 (a) illustrates the effect of varying *'hidden_layer_sizes'* on the RMSE values for the MLP model. The results indicate that *'hidden_layer_sizes'* significantly impact RMSE for both the training and testing datasets, with the optimal configuration achieved at (80, 64). Further analysis of *'learning_rate'* and *'max_iter'* parameters is shown in Fig. 9 (b) and 9 (c). It was observed that increasing the learning rate beyond 0.005

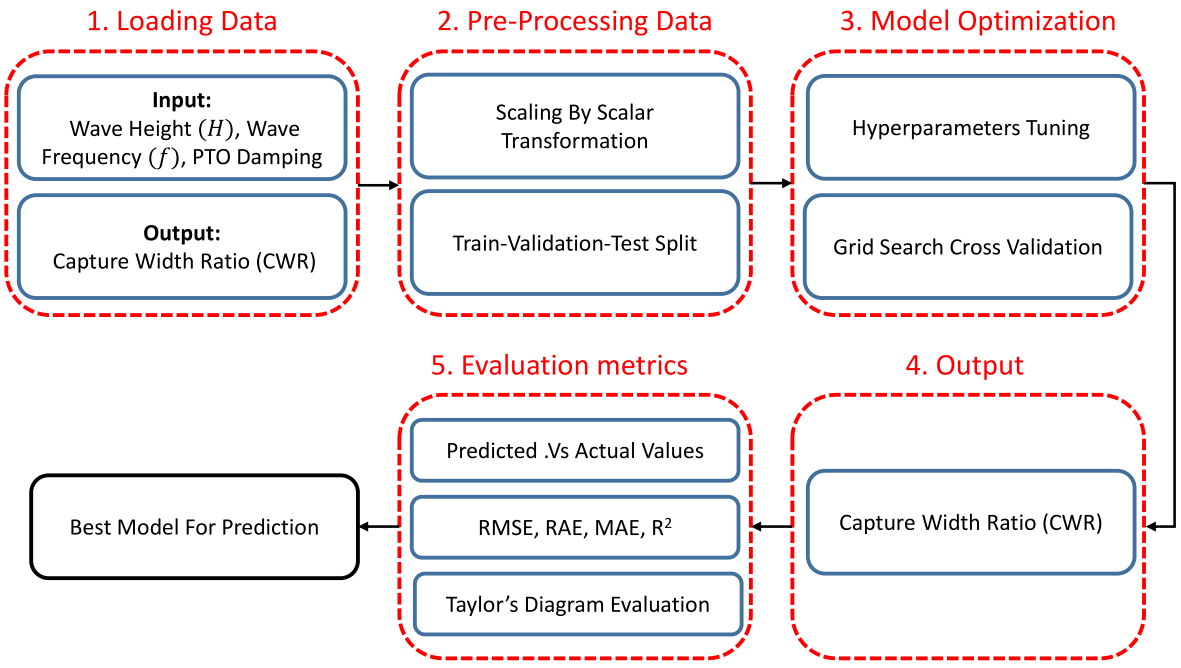

Fig. 8. Implementation of the supervised regression ML within the Framework of MBFWEC.

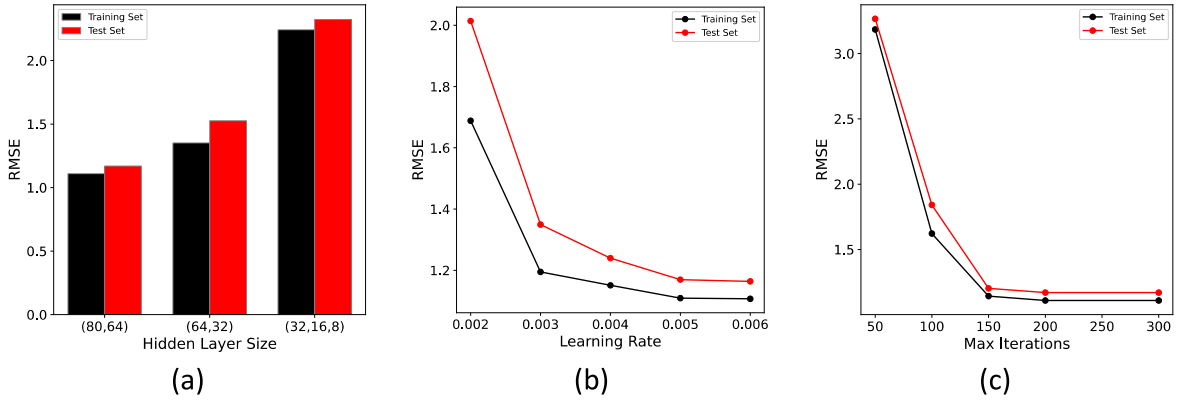

Fig. 9. Variation in MLP model hyperparameters versus train and test RMSE for (a) *'hidden_layer_sizes'*, (b) *'learning_rate'*, and (c) *'max_iter'*.

had a minimal effect on the RMSE for both training and testing sets. Similarly, increasing *'max_iter'* from 50 to 300 reduced RMSE for both datasets, with the optimal value identified at 200 iterations. Consequently, the hyperparameter tuning space for *'hidden_layer_sizes'*, *'learning_rate'*, and *'max_iter'* was constrained to these specific ranges to refine the model's performance. Our evaluation indicated that varying the activation functions and solvers did not result in substantial improvements. Therefore, *'ReLU'* and *'Adam'* were chosen as the activation function and optimization solver, respectively. This choice, along with the tuned hyperparameters listed in Table 3, mitigates the risk of overfitting while ensuring optimal model performance.

For the RF and GBRT models, hyperparameters play a pivotal role in refining the model's structure and ensuring accurate predictions. In Random Forest (RF), the *'n_estimators'* parameter represents the number of decision trees in the ensemble, where a higher number typically improves performance but increases computational overhead. The *'Max_depth'* parameter controls the depth of each tree, limiting how deeply each tree is grown. This restriction prevents the model from capturing too much detail and potentially overfitting the training data. Parameters such as *'min_sample_split'* and *'min_sample_leaf'* ensure that each node and leaf in the decision trees contain a minimum number of data samples, adding robustness to the model and reducing overfitting by preventing the creation of overly specific rules.

In GBRT, hyperparameters like *'learning_rate'* influence how much each successive tree contributes to the final model. Lower learning rates reduce overfitting and make the model more conservative, while higher learning rates can accelerate convergence at the risk of overfitting. Parameters such as *'subsample'* and *'colsample_bytree'* determine the fraction of samples and features considered for each tree, respectively, promoting generalization by introducing randomness and diversity in tree construction. This stochastic element helps prevent any single feature from dominating the model, ensuring a more balanced and generalizable solution.

Fine-tuning these hyperparameters is crucial to achieving a balance between model complexity and generalization, leading to optimal predictive performance. To this end, Grid Search Cross-Validation (GSCV) was employed with a 5-fold cross-validation strategy to systematically explore the best hyperparameter combinations for each model. This approach ensures comprehensive coverage of the hyperparameter space while simultaneously assessing model robustness by averaging performance across multiple folds. This reduces the risk of overfitting and provides a more reliable estimation of the model's performance.

Table 3
Summary of hyperparameters and optimal values for all the ML models tested in this study.

Supervised Models	Hyperparameters	Best Values
MLP	'hidden_layer_sizes': (80, 64), (64, 32), (32, 16, 8) 'activation': ('relu'), 'solver': (adam), 'batch_size': (32, 16, 8), 'learning_rate': (0.002, 0.003, 0.004, 0.005, 0.006), 'max_iter': (50, 100, 150, 200, 300)	'hidden_layer_sizes': (80, 64), 'activation': ('relu'), 'solver': (adam), 'batch_size': (16), 'learning_rate': (0.005) 'max_iter': (200)
RF	'n_estimators': (40, 50, 60, 75), 'max_depth': (5, 8, 10, 12, 15), 'min_sample_split': (4, 5, 8), 'min_sample_leaf': (4, 5, 6), 'bootstrap': (True, False)	'n_estimators': (50), 'max_depth': (10), 'min_sample_split': (5), 'min_sample_leaf': (5), 'bootstrap': (True),
GBRT	'n_estimators': (40, 50, 60), 'max_depth': (4, 5, 8, 10), 'learning_rate': (0.001, 0.01, 0.1), 'subsample': (0.5, 0.8) colsample_bytree': (0.4, 0.8, 1), 'colsample_bylevel': (0.4, 0.8, 1)	'n_estimators': (50), 'max_depth': (5), 'learning_rate': (0.01), 'subsample': (0.8), colsample_bytree': (0.4), 'colsample_bylevel': (1.0)

The details of the hyperparameters considered and the optimal values selected by GSCV for each model are presented in Table 3. Notably, a total of 1350, 1800, and 3240 fits were evaluated for MLP, RF, and GBRT models, respectively, using the 5-fold cross-validation method. These fits correspond to the unique hyperparameter combinations explored for each model. The optimal set of hyperparameters for each method was determined based on the configuration that resulted in the lowest RMSE, reflecting the best predictive accuracy and generalization capability for the given dataset.

The primary objective of this section is to determine the most accurate ML model for predicting the CWR of a MBFWEC under diverse sea conditions. These conditions include variations in wave height, frequency, and the device's Power Take-Off (PTO) damping. Fig. 10 presents a comparative evaluation of the predictive performance of several ML models, including MLP, GBRT, and RF, on an unseen test dataset. To facilitate meaningful comparisons, the figures include ± maximum error lines, based on the maximum absolute error observed within the test set.

Among the evaluated models, the MLP demonstrates superior performance, with predictions for the test data falling within a ±6.11 % error margin. By contrast, the GBRT model exhibits a maximum absolute error of 20.3 %, and the RF model reports an error of 22.6 %. Additionally, the MLP shows enhanced prediction accuracy for CWR values that are relatively rare and higher in magnitude, underscoring its capacity to generalize effectively to extreme or underrepresented data points.

To further elucidate the performance differences across the models, a suite of statistical metrics was computed for each, both on the training and the unseen test datasets. The results, summarized in Table 4, indicate that the MLP outperforms the other models across all evaluated metrics. The MLP achieves the highest coefficient of determination (R^2), with values of 0.9976 on the training set and 0.9945 on the test set, highlighting its ability to explain a substantial proportion of the variance in the data. Moreover, the MLP exhibits the lowest Root Mean Square Error (RMSE) and Mean Absolute Error (MAE), registering 1.1091 and 0.30605 on the training set, and 1.1697 and 0.41641 on the test set, respectively. These results underscore the MLP's superior accuracy and minimal prediction errors in comparison to the other models. In contrast, the RF model demonstrates lower R^2 values (0.99232 for the training set and 0.98674 for the test set) and higher RMSE and MAE scores (0.98786 and 0.35347 for the training set, and 1.80870 and 0.47994 for the test set). Similarly, the GBRT model underperforms relative to the MLP, with R^2 values of 0.98936 (training) and 0.97907 (test), and higher RMSE and MAE values, 1.26951 and 0.576126, for the training set, and 2.27244 and 0.79120 for the test set, respectively.

For a comprehensive comparative analysis, Fig. 11 presents a Taylor diagram, as introduced by Taylor (2001), which visualizes the correlation coefficient, standard deviation, and centered Root Mean Square Error (cRMSE) for each model. While all three models exhibit commendable performance, the MLP stands out with the highest correlation and standard deviation closely aligned with the reference values, indicating its superior fidelity to the actual data. The RF model also performs well, with high correlation and a nearly matching standard deviation. The GBRT model, although slightly lower in correlation and standard deviation, nonetheless displays robust predictive capability with minimal bias. Overall, the MLP model consistently demonstrates the most reliable and accurate performance in predicting the CWR values across a range of sea states and PTO damping values. Its superior generalization, particularly in the prediction of higher CWR values, positions the MLP as the preferred model for this task, offering

Table 4
Comparison of predictive ML-based models for modeling CWR values in training and testing dataset.

Supervised Models	Dataset	R^2	RMSE	MAE
MLP	Training Set	0.99676	1.1091	0.30605
	Test Set	0.99545	1.1697	0.41641
RF	Training Set	0.99232	1.28786	0.35347
	Test Set	0.98674	1.80870	0.47994
GBRT	Training Set	0. 98936	1.26951	0.576126
	Test Set	0.97907	2.27244	0.79120

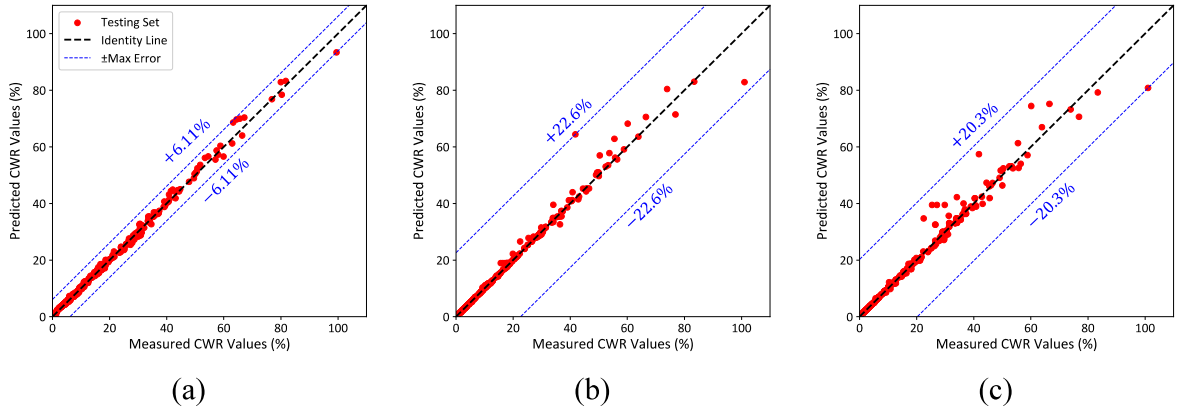

Fig. 10. Performance evaluation of supervised regression ML models for predicting CWR values (a) MLP, (b) RF, and (c) GBRT.

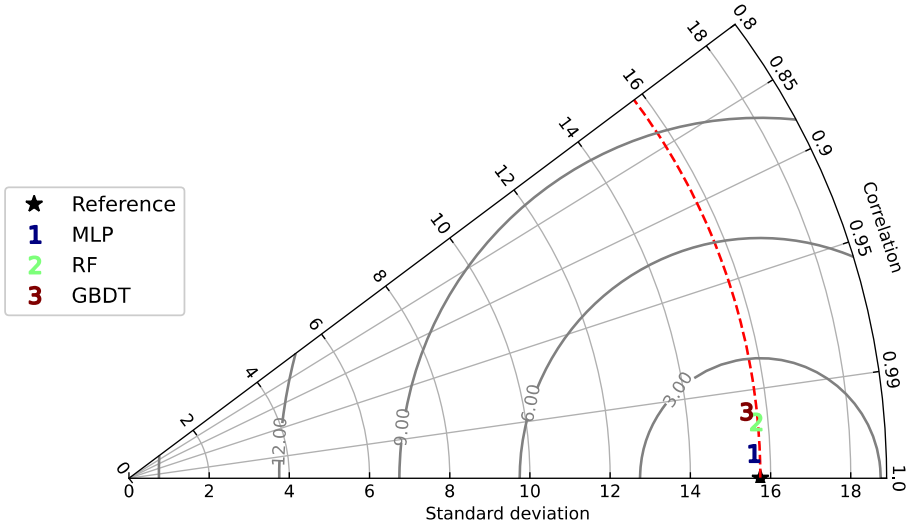

Fig. 11. Comparison of ML-based models' performance in predicting CWR.

significant potential for enhancing the predictive accuracy of WECs under real-world conditions.

Permutation feature importance analysis was conducted to evaluate the relative impact of different input features on the MLP model's prediction accuracy for the CWR. This method quantifies the importance of each input by randomly shuffling the values of one feature at a time and measuring the resulting degradation in model performance. A greater drop in performance suggests that the model is more reliant on that specific feature for making accurate predictions. As a model-agnostic approach, permutation importance offers valuable insights into the contribution of each input feature without relying on the underlying structure of the model itself. As shown in Fig. 12, wave frequency emerges as the most significant factor, displaying the highest importance score. This indicates that the model's predictive performance is highly sensitive to variations in wave frequency, with notable variability in its impact. PTO damping, while less influential than wave frequency, still exerts a consistent effect on the model's predictions. In contrast, wave height is identified as the least impactful feature, with a relatively modest importance score and moderate variability in its influence. The findings suggest that the MLP model can predict CWR values with sufficient precision, even for previously unseen or out-of-range PTO damping and wave height values. Moreover, to optimize the development of future data-driven models, the input data can be further refined by capturing wave frequency at a higher resolution, given its prominent role in prediction accuracy, while wave height can be sampled with a lower resolution due to its comparatively minimal impact. This targeted approach to dataset construction would enhance the quality of inputs and ultimately improve the model's predictive capabilities. Overall, while all three models, i.e. MLP, Random Forest, and GBRT, demonstrated strong performance, the MLP method consistently exhibited superior accuracy and reliability across multiple metrics. As a result, the MLP model was selected for further exploration and to serve as the foundation for the development of the CWR prediction window and the proposed ML-TF approach. Its exceptional performance in capturing complex patterns in the data highlights its suitability for this advanced application.

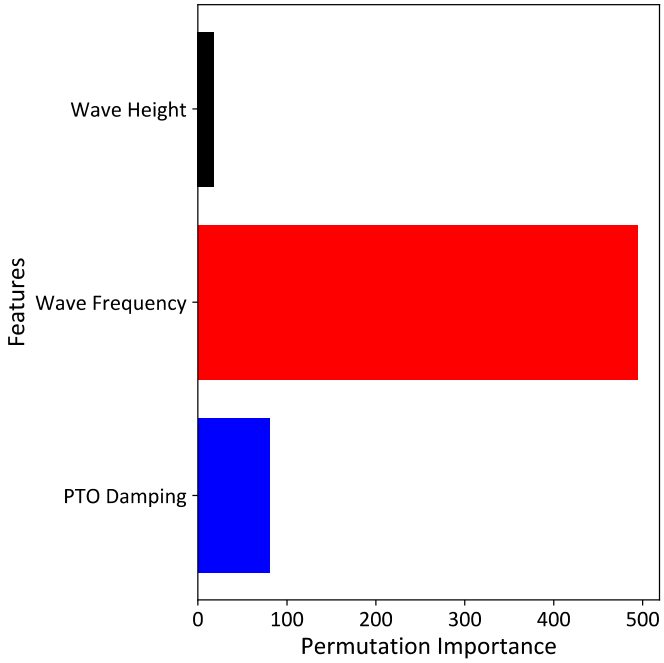

Fig. 12. Feature importance analysis for the MLP method.

3.3. Development of machine learning-transfer function (ML-TF) method

The TF concept, initially introduced by Adibzade and Akbari [15], provides a critical framework for correlating the response of a FWEC in regular wave conditions to its behavior in irregular wave environments. The essence of the TF lies in approximating the FWEC's performance under complex, irregular sea states by examining its response to a range of regular waves. By doing so, the TF enables the accurate prediction of the device's power absorption capabilities in real-world sea conditions, which are inherently more variable and dynamic than idealized regular waves. The TF is primarily dependent on wave frequency (or wave period) and can be derived from the CWR matrix. It is computed as follows:

$$TF_j = \frac{\sum_{i=1}^{m} CWR_{H_{ij}}}{m}, j = 1, 2, \ldots, n$$
$$TF = [TF_1, TF_2, \ldots, TF_n] \quad (23)$$

where m represents the number of wave heights considered in the CWR matrix, and n denotes the number of wave frequencies.

This TF is instrumental in estimating the power absorption efficiency of an FWEC device installed at a particular site. Real sea conditions are often described using the Wave Energy Spectrum (WES) $S(f)$, which represents the distribution of wave energy across different frequencies.

From this, the Wave Power Spectrum (WPS) $P(f)$, denoting the distribution of wave power over frequencies, is derived as follows:

$$P(f) = \rho g C_g(f) S(f) \tag{24}$$

$C_g(f)$ represents the wave group celerity (m/s), determined as:

$$C_g = \frac{1}{2}\sqrt{\frac{g}{k}\tanh(kd)}\left(1 + \frac{2kd}{\sinh(2kd)}\right) \tag{25}$$

where k is the wave number, and d denotes the water depth.

Utilizing the TF offers an efficient approach to estimating the total power generation of a MBFWEC. The TF, which remains constant across varying sea conditions, can be multiplied by the Wave Power Spectrum (WPS) $P(f)$, derived from the target sea state, to calculate the TAP. This process is mathematically expressed as:

$$TAP = \left(\int TF(f) \times WPS(f)\, df\right) \times l_{eff} \tag{26}$$

where l_{eff} denotes the cumulative effective length of all floating members within the MBFWEC, defined as $l_{eff} = \sum_{j=1}^{m} L_{eff_j}$, where m denotes the number of floating members in the device.

By applying this equation, the TAP of the MBFWEC is computed based on the specific TFs developed for different PTO damping levels. These TFs are systematically compared to identify the most effective PTO damping strategy for the given sea conditions, as defined by the WPS. The effectiveness of different damping strategies allows for a tailored response, ensuring optimal energy absorption under varying wave conditions. A critical aspect of this method is ensuring that the frequency resolution of the TF aligns precisely with that of the WPS, as described in Eq. (26). The accuracy of the power prediction process is heavily dependent on this match, as well as the detailed exploration of a wide range of PTO damping settings. However, this approach introduces significant computational challenges, particularly due to the need for multiple simulations to accommodate the WPS resolution and the diverse damping configurations. To mitigate these computational demands, a data-driven model, specifically using the MLP method, is employed to predict CWR matrices across a wide range of frequencies and PTO damping settings. The MLP model's predictive capabilities allow for more efficient exploration of the parameter space while maintaining high accuracy in estimating the device's performance, reducing the need for extensive numerical simulations.

Fig. 13 illustrates the CWR matrix predicted by the MLP model for a PTO damping value of 8 MNms/rad, which was not included in the model's initial training dataset. Notably, the MLP model significantly enhances the frequency-domain resolution of the CWR matrix. Using the trained MLP, the CWR matrices were generated for a frequency range between 0.02 and 0.49 Hz in 0.01 Hz increments, covering fourteen distinct PTO damping values, spaced at 2 MNms/rad intervals.

Fig. 14 presents the TFs derived from the predicted CWR matrices. Panel (a) includes TFs for PTO damping values within the training dataset; panel (b) shows TFs for values not included in the training but within the same range; and panel (c) illustrates TFs for out-of-range values. All TFs were calculated with a 0.01 Hz frequency resolution, demonstrating the MLP model's capacity to maintain high spectral resolution across a wide range of input conditions.

Achieving this 0.01 Hz frequency resolution over the specified ranges of wave height and PTO damping through conventional numerical simulations would require approximately 768 simulations per damping value. For fourteen damping values, this results in a total of 10,752 simulations. In contrast, the proposed MLP-based surrogate model was trained using only 2112 simulations and subsequently employed to generate high-resolution outputs across the entire parameter space. This represents an approximate 80 % reduction in computational cost. This substantial efficiency gain underscores the practical value of the MLP model as a surrogate tool for predicting FWEC performance. It enables rapid, high-resolution analysis across a broad spectrum of operating conditions, making it well-suited for design optimization, control strategy development, and operational studies.

A comparative analysis was performed to evaluate the accuracy of the ML-TF method by comparing it against direct time-history simulations, a conventional approach for assessing the performance of FWECs. The direct method involves solving time-domain equations to determine the device's response to irregular waves. This process begins by generating water level variations based on the WES. After this, the equations of motion for the MBFWEC are resolved. In this study, two distinct WES types were considered: a single-peak WES (WPS #1) and a double-peak WES (WPS #2), as illustrated in Fig. 15. A 3600-s time series of sea surface elevation was generated for each WES to simulate the irregular wave conditions. To maintain consistency across the simulations, the random wave phase was seeded, allowing the same random phase to be replicated in each case.

The MBFWEC configuration was simulated under these irregular wave conditions using four different PTO damping values, 8, 12, 16, and 20 MNms/rad, at a time step of 0.005 s. The computational cost of these direct simulations varied depending on the complexity of the WES, the binning of the wave spectrum (where the wave energy spectrum is divided into bins of equal energy), and the PTO damping values, which influence the hydrodynamic behaviour of the WEC. Despite the variability in computational demands, each simulation required between 3 and 4.5 h, with more complex WES cases and higher PTO damping values demanding more time. In contrast, the ML-TF method offers a more computationally efficient alternative. Using this approach, the TAP for the same scenarios was calculated following Eq. (26). This process, depicted in Fig. 15, involves multiplying the WPS by the TF and the effective length (l_{eff}) of the MBFWEC. The ML-TF method significantly reduces computational costs while still delivering accurate power predictions, as it bypasses the need for time-consuming direct

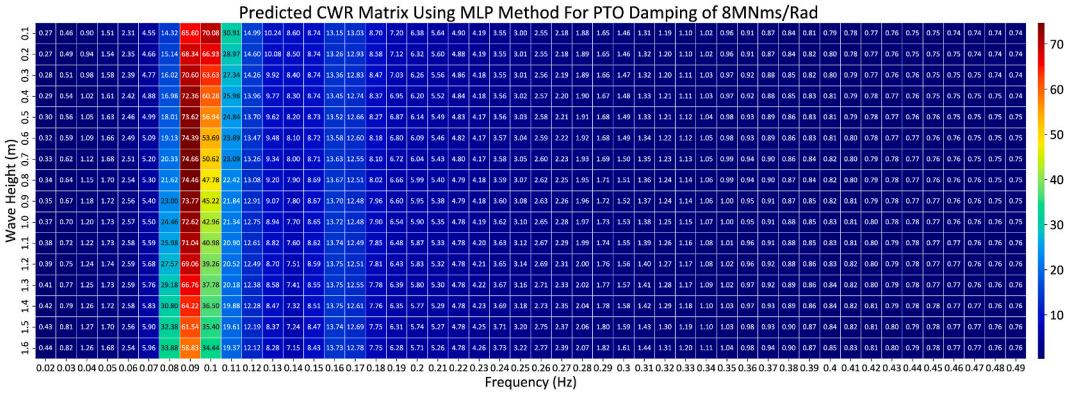

Fig. 13. Predicted CWR matrix using MLP method for PTO damping of 8MNms/rad.

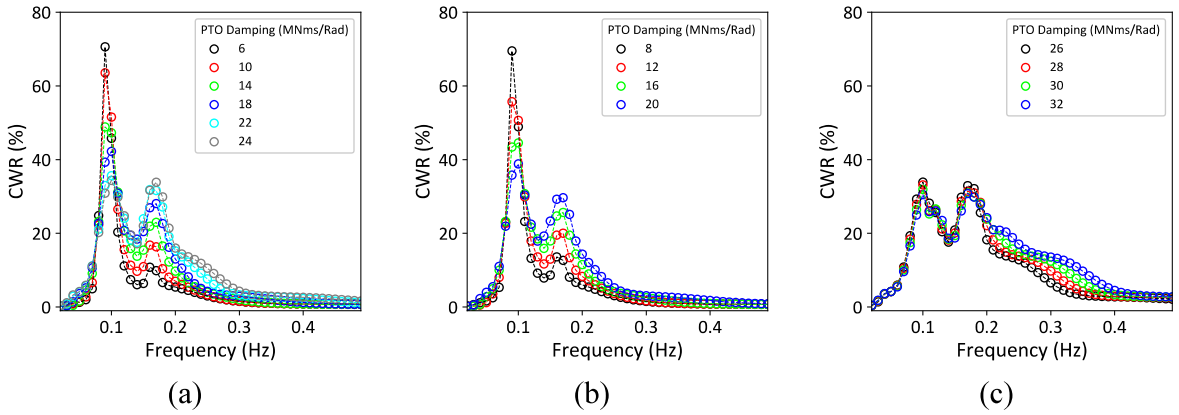

Fig. 14. TFs derived from the CWR matrices predicted using the MLP method: (a) TFs corresponding to PTO damping values included in the training dataset, (b) TFs for damping values that were not included in the training dataset but fall within the input PTO damping range, and (c) TFs for out-of-range PTO damping values.

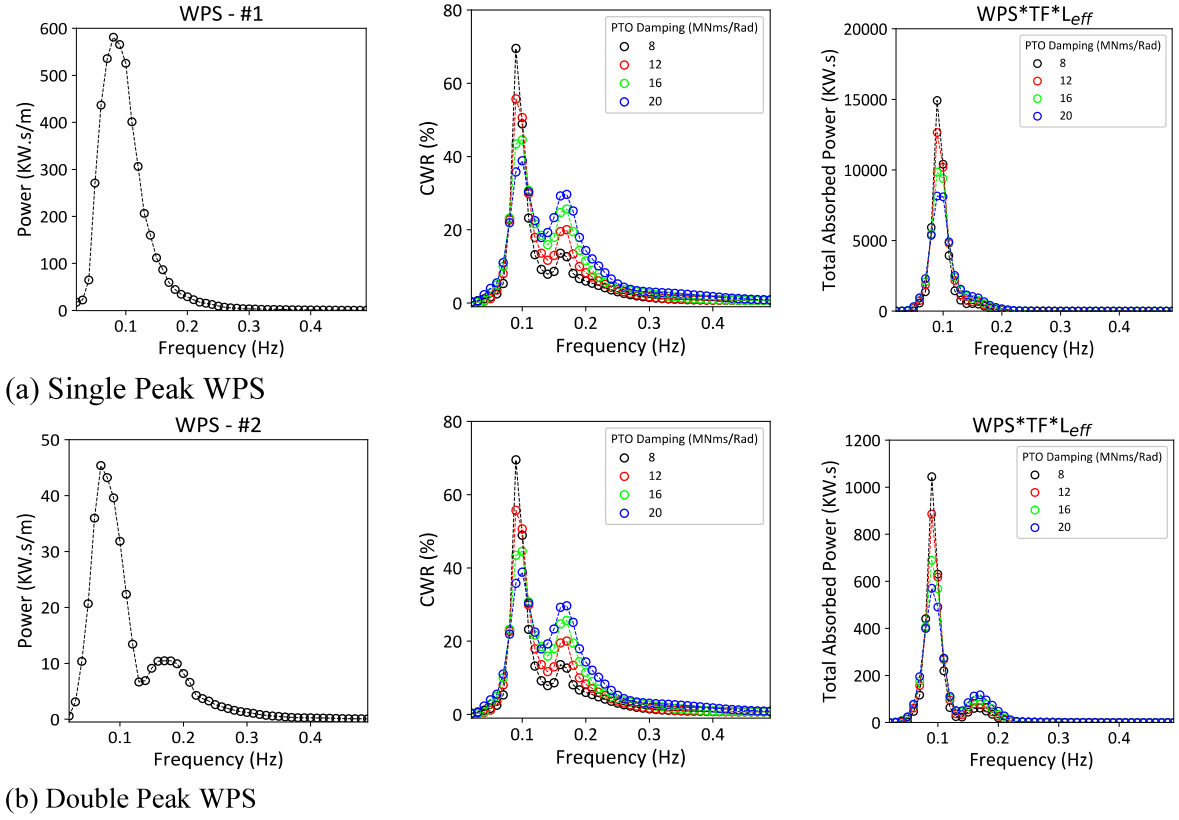

Fig. 15. The procedural framework for developing the TAP function for a MBFWEC. This process is based on integrating the WPS with the TF across various PTO damping scenarios.

simulations.

Table 5 presents the calculated TAP values obtained through both the direct time-history simulations and the ML-TF method. The results demonstrate that the proposed ML-TF method delivers highly accurate estimates of TAP across both single-peak and double-peak WPS. Remarkably, the maximum deviation between the two methods is less than 4 %, underscoring the precision and reliability of the ML-TF approach. This minor deviation indicates that the ML-TF method not only reduces the computational burden associated with direct time-history simulations but also maintains a high level of accuracy.

To further evaluate the accuracy of the ML-TF method in predicting the TAP for sea states with PTO damping values not included in the initial training dataset, we extended the comparative analysis to damping values of 26, 28, 30, and 32 MNms/rad. TFs for these damping values, predicted by the MLP model, are presented in Fig. 14 (c).

Table 6 compares the TAP results obtained from direct time-history simulations with those estimated by the ML-TF method. The maximum observed error between the two approaches is less than 8 %, demonstrating the robustness and adaptability of the ML-TF method, even for damping values outside the original dataset range. As previously discussed, the MLP model's prediction and, by extension, the ML-TF method's accuracy, exhibits low sensitivity to changes in PTO damping (as indicated in Fig. 12). The results of this extended comparative analysis support that observation. However, it is important to note that while the ML-TF method remains highly accurate, the error tends to increase slightly as the damping values deviate further from

Table 5
Comparison of the TAP computed using the Direct Time-Domain and the ML-TF methods for damping values that were not included in the training dataset but fall within the input PTO damping range.

Model	WPS	PTO Damping $\left(\frac{MNms}{rad}\right)$	$TAP_{Time\ History}$	$TAP_{ML\text{-}TF}$	Error (%)
1	WPS #1	8	395.7	411.7	4.0
2	WPS #1	12	405.7	420.7	3.7
3	WPS #1	16	403.1	410.3	1.8
4	WPS #1	20	392.7	392.8	0.03
5	WPS #2	8	29.3	28.5	2.8
6	WPS #2	12	29.8	29.4	1.4
7	WPS #2	16	29.9	29.3	2.2
8	WPS #2	20	29.9	28.9	3.4

Table 6
Comparison of the TAP computed using the Direct Time-Domain and the ML-TF methods for out-of-range PTO damping values.

Model	WPS	PTO Damping $\left(\frac{MNms}{rad}\right)$	$TAP_{Time\ History}$	$TAP_{ML\text{-}TF}$	Error (%)
1	WPS #1	26	373.0	369.0	1.1
2	WPS #1	28	366.2	360.1	1.7
3	WPS #1	30	359.5	351.2	2.3
4	WPS #1	32	352.9	343.1	2.8
5	WPS #2	26	29.7	28.3	4.6
6	WPS #2	28	29.6	28.0	5.5
7	WPS #2	30	29.5	27.5	6.7
8	WPS #2	32	29.4	27.0	8.0

those within the original training dataset. Despite this, the deviation remains within acceptable bounds, further validating the ML-TF approach's capability to generalize well to out-of-range damping values while maintaining efficient and precise power prediction for the MBFWEC system.

3.4. Application of ML-TF method for a case study of Oman sea

The ML-TF method for estimating the TAP was applied to a real-world case study using wave data from the Makran region, situated in the northern part of the Oman Sea. This region's wave data was sourced from wave measurements conducted in 2016 by the Iranian Port and Maritime Organization (PMO). Nortek Acoustic Wave and Current (AWAC) instruments were deployed at multiple stations along the southern coastal area of Balochistan province to monitor wave conditions. Specifically, data from seven stations (illustrated in Fig. 16) provided detailed insight into various sea states. For the purposes of this case study, we focused on wave data from three key stations: Meydani, Pozm, and Pasabandar. These locations were chosen because they offer broad coverage of the Makran coastline. Detailed information on the selected stations is provided in Table 7.

The AWAC instruments gathered sea surface elevation and wave particle velocity data (u, v) at intervals of 1024 s per hour. Nortek's Storm V1.14 software was then employed to process this data and derive the WES $S(f)$ for each observed sea state, which formed the foundation for this study. The Oman Sea, as depicted in Fig. 16, is subject to two distinct wave systems, one originating from the west and the other from the south. These systems create complex wave conditions, making the region an ideal location to evaluate the performance and robustness of the ML-TF approach. Data collection in the Makran region began in February 2016 and continued through November/December, allowing the dataset to capture the region's varying climatic conditions, which are heavily influenced by the monsoon seasons [36].

The South-West (summer) monsoon, lasting from June to September, is associated with the highest wave energy in the region, characterized by strong wave activity and intense sea states. Conversely, the post-monsoon period (October to January) and the pre-monsoon period (February to May) are defined by calmer conditions and lower wave energy. This temporal variation provided a comprehensive dataset to evaluate the TAP predictions under a wide range of sea states using the ML-TF method. The case study demonstrates the versatility and effectiveness of the ML-TF method in real-world applications, showcasing its ability to accurately estimate the TAP across varying climatic conditions and wave energy spectra. By leveraging the MLP-predicted TFs and wave data from the Oman Sea, the method proved highly capable of capturing the dynamic behaviour of FWEC systems under realistic and complex sea conditions. This underscores its potential for broader application in coastal energy projects.

A total of 209 sea state samples were analysed to estimate the TAP of the proposed MBFWEC across three locations: Meydani, Pozm, and Pasabandar. The selected wave conditions encompassed a broad spectrum of spectral characteristics, including uni-modal, bi-modal, and multi-modal sea states, corresponding to single-peak, double-peak, and multi-peak WES profiles, respectively. Utilizing ten distinct TFs, each corresponding to a specific PTO damping value, the ML–TF approach was applied across all sea state samples to produce high-resolution TAP predictions. This approach facilitated a detailed examination of the power absorption performance of the MBFWEC under a wide range of sea state complexities and PTO configurations, providing insights into its operational robustness and adaptability across diverse marine environments.

Fig. 17 presents the TAP results for all analysed sea states, organized chronologically by date, across the full range of PTO damping levels. This figure provides a comprehensive overview of the system's performance over time and across varying energy regimes. A clear seasonal pattern is evident: TAP values are consistently higher during the South-West monsoon season (June to September), with the most pronounced increases observed at the Pasabandar station. This enhancement corresponds to the seasonal arrival of long-period swell waves from the Arabian Sea and Oman Sea, which significantly elevate the regional wave energy potential. These swell waves, characterized by higher group velocities (C_g), contribute to enhanced energy capture efficiency by promoting stronger and more coherent wave-body interactions. In contrast, the Meydani station, dominated by shorter-period, wind-driven waves from the Persian Gulf, exhibits lower TAP values despite experiencing similar or even higher significant wave heights. This reduced performance stems from the lower C_g associated with local wind-generated waves, which carry less energy per unit wave height compared to swell-dominated conditions. The Pozm station displays intermediate behavior, with TAP values reflecting the combined influence of both swell- and wind-dominated sea states throughout the year.

Fig. 17 also highlights the system's sensitivity to PTO damping. For each sea state, the TAP curves exhibit distinct peaks, identifying the optimal damping value for maximum energy absorption. Two primary trends emerge from the analysis. First, during low-energy periods (typically February–May and October–January), the optimal TAP is achieved at higher PTO damping values, approximately 24 MN m s/rad. Second, during the South-West monsoon season, when sea states are

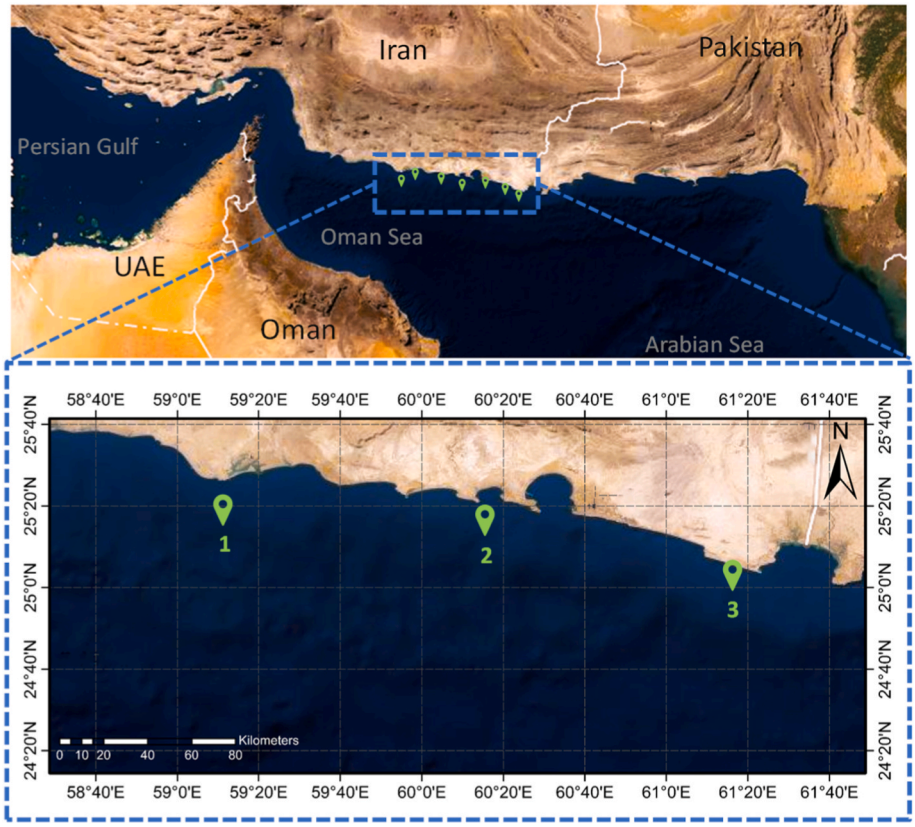

Fig. 16. Location of wave data measurement stations along the Makran coast in the northern part of the Oman Sea.

Table 7
Summary of wave data measurement stations.

Station No.	Name	Depth (m)	Latitude (DMS)	Longitude (DMS)	Measurement period
1	Meydani	30	25° 16′ 37″	59° 11′ 45″	Feb–Nov 2016
2	Pozm	30	25° 13′ 36″	60° 15′ 02″	Feb–Dec 2016
3	Pasabandar	30	24° 56′ 86″	61° 18′ 74″	Feb–Dec 2016

more energetic, lower damping values near 10 MN m s/rad yield superior performance. These transitions are clearly reflected in the damping-specific TAP profiles presented in the figure. The ability to accurately identify and adapt to seasonal variations in optimal damping is essential for maximizing energy capture and operational efficiency throughout the year. This finding underscores the importance of adaptive PTO control strategies in enhancing the long-term performance of wave energy converters across diverse sea states.

4. Conclusion

This study presents a novel ML-TF approach for accurately estimating the TAP of FWECs under complex sea conditions. The proposed methodology integrates physics-based numerical modelling with supervised ML, enabling robust TAP predictions while achieving a substantial reduction in computational cost. This efficiency facilitates extensive scenario modelling, detailed performance assessment, and optimization of FWECs across diverse operational and environmental conditions.

The proposed process begins with frequency-domain modelling based on potential flow theory to extract hydrodynamic coefficients. These are followed by time-domain simulations using WEC-Sim to capture the FWEC's dynamic response under a range of regular wave conditions. The resulting CWR matrices form the training dataset for ML algorithms, including Random Forest (RF), Gradient Boosted Regression Trees (GBRT), and Multi-Layer Perceptron (MLP). The optimized MLP model generates high-resolution CWR windows across a range of PTO damping values and frequencies. These outputs are used to construct TFs, which enable efficient and accurate TAP estimations across arbitrary sea states by incorporating region-specific wave energy spectra (WES).

Compared to conventional numerical simulation methods, the ML–TF framework achieves an approximate 80 % reduction in computational cost while maintaining high predictive accuracy. Validation against direct time-history simulations under both single-peak and double-peak sea states yielded maximum errors of less than 4 % for in-range PTO damping values, and under 8 % for extrapolated values. These results confirm the model's robustness and generalizability, even when predicting beyond the original training set. Key advantages of the ML–TF approach include its hybrid nature, which retains the physical interpretability of TFs while leveraging the predictive capabilities of ML. Moreover, it enables the generation of high-resolution outputs from relatively sparse datasets, making it an efficient and practical surrogate model for FWEC performance prediction.

Application of the model to the northern Oman Sea, utilizing 209 observed sea states, revealed important regional performance insights. Ten distinct TFs were developed for various PTO damping levels to estimate TAP and identify optimal damping strategies. Among the sites studied, Pasabandar exhibited the highest power potential, particularly during the summer monsoon when long-period swell waves dominate. In contrast, Meydani, predominantly influenced by shorter-period, wind-generated waves, demonstrated lower energy availability, while Pozm displayed intermediate performance reflecting a blend of wave climates. Analysis further confirmed that swell-dominated sea states yield higher energy capture efficiency, whereas low-energy conditions

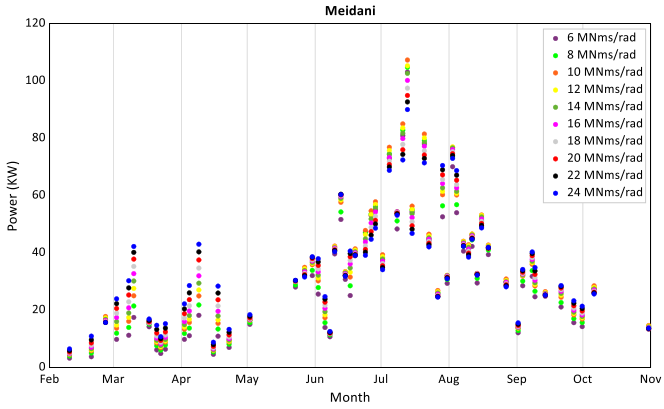

(a)

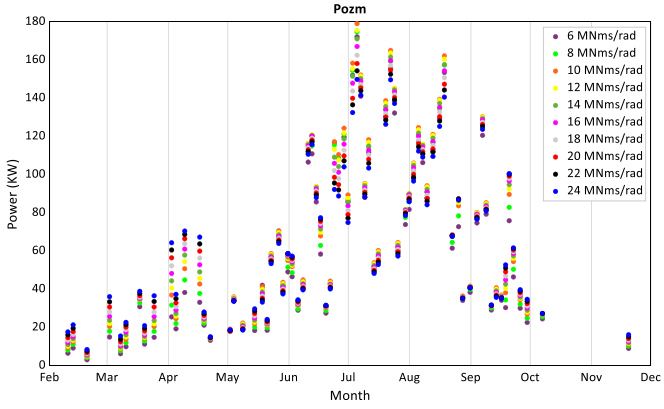

(b)

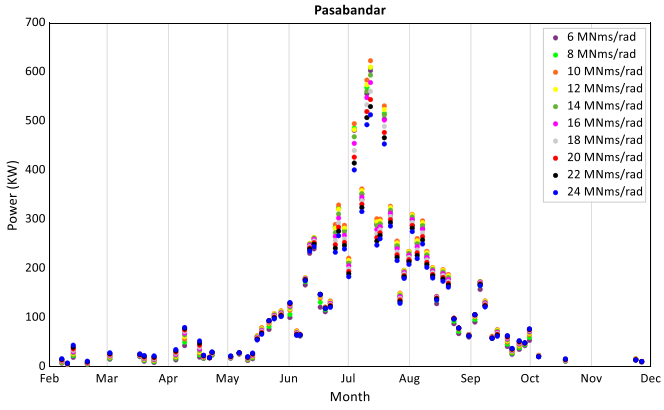

(c)

Fig. 17. TAP of the proposed MBFWEC across different sea states, categorized by occurrence date at (a) Meydani, (b) Pozm, and (c) Pasabandar stations.

benefit from higher PTO damping values, while high-energy conditions favour lower damping.

Noted limitations of the proposed framework include its dependence on the quality and diversity of the training dataset, reduced accuracy when extrapolating far beyond the trained PTO damping or wave frequency ranges, and the assumption of unidirectional sea states in its current implementation. Future research will aim to extend the ML–TF approach to incorporate wave directionality, a factor known to significantly influence TAP, as demonstrated in prior studies. While modelling broadband, directionally distributed irregular waves poses substantial computational challenges, integrating ML into this context offers substantial potential to enhance efficiency. Expanding the framework to account for directional spreading will allow for a more comprehensive and realistic evaluation of FWEC performance under naturally occurring sea conditions.

CRediT authorship contribution statement

Mohammadreza Torabbeigi: Writing – original draft, Visualization, Validation, Software, Methodology, Investigation, Formal analysis, Data curation, Conceptualization. **Mohammad Adibzade:** Writing – original draft, Visualization, Software, Methodology, Formal analysis, Data curation. **Arash Baharifar:** Writing – original draft, Visualization, Methodology, Data curation. **Soroush Abolfathi:** Writing – review & editing, Writing – original draft, Visualization, Validation, Supervision, Resources, Project administration, Methodology, Investigation, Funding acquisition, Conceptualization.

Declaration of competing interest

The authors declare that they have no known competing financial interests or personal relationships that could have appeared to influence the work reported in this paper.

Acknowledgements

The authors would like to thank Dr Hassan Akbari for their support and advise throughout this study. SA acknowledges resources and support from the Scientific Computing Research Technology Platform (SCRTP) at the University of Warwick and the Natural Environment Research Council (NE/S007350/1).

Nomenclature

CWR	Capture Width Ratio
DOF	Degree of Freedom
FWEC	Floating Wave Energy Converter
GBRT	Gradient Boosted Regression Tree
MAE	Mean Absolute Error
MBFWEC	Multi Body Floating Wave Energy Converter
MLP	Multi-Layer Perceptron
ML	Machine Learning
PTO	Power Take-Off
R^2	Coefficient of Determination
RAE	Relative Absolute Error
RF	Random Forest
RMSE	Root Mean Square Error
TAP	Total Absorbed Power
TF	Transfer Function
WEC	Wave Energy Converter
WES	Wave Energy Spectrum
WPS	Wave Power Spectrum

Appendix A. Supplementary data

Supplementary data to this article can be found online at https://doi.org/10.1016/j.renene.2025.125011.

References

[1] V. Manimegalai, V. Rukkumani, A. Gayathri, P. Pandiyan, V. Mohanapriya, An overview of global renewable energy resources, Renew. Energy AI Sustain. Dev. 2 (2.4) (2023) 2–5.
[2] H.H.H. Aly, A novel deep learning intelligent clustered hybrid models for wind speed and power forecasting, Energy 213 (2020) 118773.
[3] A. Azam, et al., Wave energy evolution: knowledge structure, advancements, challenges and future opportunities, Renew. Sustain. Energy Rev. 205 (2024) 114880, https://doi.org/10.1016/j.rser.2024.114880.
[4] M. O'connor, T. Lewis, G. Dalton, Techno-economic performance of the Pelamis P1 and Wavestar at different ratings and various locations in Europe, Renew. Energy 50 (2013) 889–900.
[5] A. De Andres, J. Maillet, J. Hals Todalshaug, P. Möller, D. Bould, H. Jeffrey, Techno-economic related metrics for a wave energy converters feasibility assessment, Sustainability 8 (11) (2016) 1109.
[6] M. Adibzade, H. Akbari, Fully spectral approach to evaluate the performance of floating wave energy converters in directional complex sea states, Ocean Eng. 306 (2024) 117999, https://doi.org/10.1016/j.oceaneng.2024.117999.
[7] J. Tan, H. Polinder, A.J. Laguna, P. Wellens, S.A. Miedema, The influence of sizing of wave energy converters on the techno-economic performance, J. Mar. Sci. Eng. 9 (1) (2021) 52.
[8] S. Chandrasekaran, V.V.S. Sricharan, Numerical study of bean-float wave energy converter with float number parametrization using WEC-Sim in regular waves with the Levelized Cost of Electricity assessment for Indian sea states, Ocean Eng. 237 (2021) 109591.
[9] B. Tagliafierro, et al., A numerical study of a taut-moored point-absorber wave energy converter with a linear power take-off system under extreme wave conditions, Appl. Energy 311 (2022) 118629.
[10] J. Tan, H. Polinder, A.J. Laguna, S. Miedema, The application of the spectral domain modeling to the power take-off sizing of heaving wave energy converters, Appl. Ocean Res. 122 (2022) 103110.
[11] R. Suchithra, K. Ezhilsabareesh, A. Samad, Development of a reduced order wave to wire model of an OWC wave energy converter for control system analysis, Ocean Eng. 172 (2019) 614–628.
[12] Y. Wei, A. Bechlenberg, M. van Rooij, B. Jayawardhana, A.I. Vakis, Modelling of a wave energy converter array with a nonlinear power take-off system in the frequency domain, Appl. Ocean Res. 90 (2019) 101824.
[13] H. Zhou, Y. Qiu, Y. Feng, J. Liu, Power prediction of wind turbine in the wake using hybrid physical process and machine learning models, Renew. Energy 198 (2022) 568–586.
[14] C. Ren, J. Tan, Y. Xing, ALK-PE: an efficient active learning Kriging approach for wave energy converter power matrix estimation, Ocean Eng. 286 (2023) 115566.
[15] M. Adibzade, H. Akbari, Spectral approach to evaluate multi-body floating wave energy converters in complex sea states, Ocean Eng. 286 (2023) 115567.

[16] D. Ogden, et al., Review of WEC-Sim development and applications, Int. Mar. Energy J. 5 (NREL/JA-5700–83366) (2022).
[17] W.E. Cummins, others, The Impulse Response Function and Ship Motions, 1962.
[18] T. Jiang, J.L. Gradus, A.J. Rosellini, Supervised machine learning: a brief primer, Behav. Ther. 51 (5) (2020) 675–687.
[19] K. Khosravi, A.A. Farooque, M. Karbasi, et al., Enhanced water quality prediction model using advanced hybridized resampling alternating tree-based and deep learning algorithms, Environ. Sci. Pollut. Res. 32 (2025) 6405–6424. https://doi.org/10.1007/s11356-025-36062-7.
[20] P. Kent, S. Abolfathi, H. Al Ali, T. Sedighi, O. Chatrabgoun, A. Daneshkhah, Resilient coastal protection infrastructures: probabilistic sensitivity analysis of wave overtopping using Gaussian process surrogate models, Sustainability 16 (20) (2024) 9110. https://doi.org/10.3390/su16209110.
[21] M.A. Habib, J.J. O'Sullivan, S. Abolfathi, M. Salauddin, Enhanced wave overtopping simulation at vertical breakwaters using machine learning algorithms, PLoS One 18 (8) (2023) e0289318.
[22] M. Riazi, S.M. Bateni, C. Jun, A.A. Farooque, K. Khosravi, S. Abolfathi, Enhancing rainfall-runoff simulation in data-poor watersheds: integrating remote sensing and hybrid decomposition for hydrologic modelling, Water Res. Manag. (2025) 1–26.
[23] M.A. Habib, S. Abolfathi, J.J. O'Sullivan, P.R. Brooks, M. Salauddin, Advancing wave overtopping prediction at eco-engineered Seawalls: Integrating laboratory experiments and machine learning, Ocean Eng 340 (2025) 122284.
[24] B.-L. Dang, H. Nguyen-Xuan, M. Abdel Wahab, An effective approach for VARANS-VOF modelling interactions of wave and perforated breakwater using gradient boosting decision tree algorithm, Ocean Eng. 268 (2023) 113398, https://doi.org/10.1016/j.oceaneng.2022.113398.
[25] C. Chen, W. He, H. Zhou, Y. Xue, M. Zhu, A comparative study among machine learning and numerical models for simulating groundwater dynamics in the Heihe River Basin, northwestern China, Sci. Rep. 10 (1) (2020) 3904.
[26] K. Khosravi, N. Attar, S.M. Bateni, C. Jun, D. Kim, M.J. Safari, S. Heddam, A. Farooque, S. Abolfathi, Daily river flow simulation using ensemble disjoint aggregating M5-Prime model, Heliyon 10 (20) (2024).
[27] L. Breiman, Random forests, Mach. Learn. 45 (2001) 5–32.
[28] J.H. Friedman, Greedy function approximation: a gradient boosting machine, Ann. Stat. (2001) 1189–1232.
[29] D. Sarkar, R. Bali, T. Ghosh, Hands-On Transfer Learning with Python: Implement Advanced Deep Learning and Neural Network Models Using Tensorflow and Keras, Packt Publishing Ltd, 2018.
[30] J.V. Ringwood, G. Bacelli, F. Fusco, Energy-maximizing control of wave-energy converters: the development of control system technology to optimize their operation, IEEE Control Syst. Mag. 34 (5) (2014) 30–55.
[31] J. Falnes, Wave-Energy Conversion Through Relative Motion Between Two single-mode Oscillating Bodies, 1999.
[32] M.J. French, R.H. Bracewell, PS Frog a point-absorber Wave Energy Converter Working in a pitch/surge Mode, 1987.
[33] S. Chandrasekaran, V.V.S. Sricharan, Numerical analysis of a new multi-body floating wave energy converter with a linear power take-off system, Renew. Energy 159 (2020) 250–271.
[34] ANSYS Inc, ANSYS AQWA User's Manual, 2023. Canonsburg, PA.
[35] K. Budar, J. Falnes, A resonant point absorber of ocean-wave power, Nature 256 (5517) (1975) 478–479.
[36] M. Adibzade, M. Shafieefar, H. Akbari, R. Panahi, Multi-peaked directional wave spectra based on extensive field measurement data in the Gulf of Oman, Ocean Eng. 230 (2021) 109057.